OPEN ACCESS



Probing the Diffuse Ly α Emission on Cosmological Scales: Ly α Emission Intensity Mapping Using the Complete SDSS-IV eBOSS

Xiaojing Lin¹, Zheng Zheng², and Zheng Cai¹
Department of Astronomy, Tsinghua University, Beijing 100084, People's Republic of China; zcai@mail.tsinghua.edu.cn
Department of Physics and Astronomy, University of Utah, UT 84112, USA; zhengzheng@astro.utah.edu

Received 2022 April 6; revised 2022 July 16; accepted 2022 July 19; published 2022 September 20

Abstract

Based on Sloan Digital Sky Survey Data Release 16, we have detected the large-scale structure of Ly α emission in the universe at redshifts z=2–3.5 by cross-correlating quasar positions and Ly α emission imprinted in the residual spectra of luminous red galaxies. We apply an analytical model to fit the corresponding Ly α surface brightness profile and multipoles of the redshift-space quasar–Ly α emission cross-correlation function. The model suggests an average cosmic Ly α luminosity density of $6.6^{+3.3}_{-3.1} \times 10^{40}$ erg s⁻¹ cMpc⁻³, a ~2 σ detection with a median value about 8–9 times those estimated from deep narrowband surveys of Ly α emitters at similar redshifts. Although the low signal-to-noise ratio prevents us from a significant detection of the Ly α forest–Ly α emission cross-correlation, the measurement is consistent with the prediction of our best-fit model from quasar–Ly α emission cross-correlation within current uncertainties. We rule out the scenario where the Ly α photons mainly originate from quasars. We find that Ly α emission from star-forming galaxies, including contributions from that concentrated around the galaxy centers and that in diffuse Ly α -emitting halos, is able to explain the bulk of the Ly α luminosity density inferred from our measurements. Ongoing and future surveys can further improve the measurements and advance our understanding of the cosmic Ly α emission field.

Unified Astronomy Thesaurus concepts: Intergalactic medium (813); Lyman-break galaxies (979); Galaxies (573); Lyman-alpha galaxies (978); Intergalactic filaments (811)

1. Introduction

The filamentary structure of the cosmic web, which links galaxies to the intergalactic medium (IGM), is predicted to be a rich reservoir of nearly pristine gas (e.g., Fumagalli et al. 2011; Giavalisco et al. 2011). Reprocessed radiation from quasars or the ultraviolet (UV) background will ionize hydrogen atoms in the circumgalactic medium (CGM) and IGM (e.g., Borisova et al. 2016; Gallego et al. 2021; Lujan Niemeyer et al. 2022), and the recombination of the ionized hydrogen will produce fluorescent Ly α emission, especially in the high-redshift universe (Cantalupo et al. 2008; Li et al. 2021). Extended Ly α emission is expected due to the large cross section of Ly α photons for resonant scatterings by neutral hydrogen (Zheng et al. 2011a).

Direct imaging of the IGM Ly α emission is challenging because of its low surface brightness (SB) (Cantalupo et al. 2005). One solution is to search around local ionized sources, such as luminous quasars, which reside at the densest regions of the cosmic web. The diffuse gas emission can be enhanced by orders of magnitude, leading to the discovery of enormous Ly α nebulae (Cantalupo et al. 2014; Hennawi et al. 2015; Cai et al. 2017, 2018; Arrigoni Battaia et al. 2018). These extrema of Ly α nebulosities have Ly α SB $\geqslant 10^{-17}$ erg s⁻¹ cm⁻² arcsec⁻² and Ly α luminosity $\geqslant 10^{44}$ erg s⁻¹, with Ly α sizes greater than 200 kpc. Recently, the progress in wide-field integral field spectrographs has extended the detectability of CGM/IGM with low SB. The most advanced facilities, such as the Keck Cosmic Web Imager (KCWI; Morrissey et al. 2018) and the Multi Unit Spectroscopic

Original content from this work may be used under the terms of the Creative Commons Attribution 4.0 licence. Any further distribution of this work must maintain attribution to the author(s) and the title of the work, journal citation and DOI.

Explorer (MUSE; Bacon et al. 2010), can reach an SB of a few $\times 10^{-19}$ erg s⁻¹ cm⁻² arcsec⁻², making it possible to conduct observational probes into emission from the CGM/IGM in the vicinity of bright sources (KCWI: Arrigoni Battaia et al. 2016; Borisova et al. 2016; Cai et al. 2019, etc.; MUSE: Wisotzki et al. 2018; Bacon et al. 2021; Kusakabe et al. 2022, etc.). Large numbers of individual Ly α halos around strong Ly α emitters (LAEs) have been detected thanks to these state-of-the-art instruments (e.g., Wisotzki et al. 2016; Leclercq et al. 2017). Moreover, a recent discovery unveiled that star-forming galaxies generally have Ly α halos by investigating Ly α emission around UV-selected galaxies (Kusakabe et al. 2022).

On scales up to several Mpc from the central bright sources, no direct observational evidence for diffuse gas emissions has been found so far. The predicted Ly α SB at $z \ge 3$ stimulated by the diffuse ionizing background is on the order of 10^{-20} erg s⁻¹ cm⁻² arcsec⁻² (Gould & Weinberg 1996; Cantalupo et al. 2005; Kollmeier et al. 2010; Witstok et al. 2021). Currently, this goes far beyond the capability of the most advanced instruments on individual detections. The technique of line intensity mapping (Kovetz et al. 2017) is expected to exceed current observational limits, by mapping large-scale structures with integrated emission from spectral lines originating from galaxies and the diffuse IGM, but without resolving discrete objects. Its application on 21 cm HI emission has revealed promising prospects for observing the low-density cosmic web (Masui et al. 2013; Anderson et al. 2018; Tramonte et al. 2019; Tramonte & Ma 2020).

Ly α lines can also be used for intensity mapping (IM). Ly α IM experiments can provide viable complementary approaches to testing many theoretical predictions on the diffuse emission from IGM filaments (Silva et al. 2013, 2016; Heneka et al. 2017; Elias et al. 2020), bringing new insights into the

evolution of the universe independently of cosmological hydrodynamic simulations (Croft et al. 2016, 2018; Gallego et al. 2018, 2021). Croft et al. (2016) measured the large-scale structure of Ly α emission by the cross-correlation between Ly α SB extracted from the spectra of luminous red galaxies (LRGs) and that extracted from the spectra of quasars in the Sloan Digital Sky Survey (SDSS)/Baryon Oscillation Spectroscopic Survey (BOSS). If the Ly α emission originates from star formation in faint Ly α -emitting galaxies, the star formation rate density (SFRD) inferred from the measurement would be \sim 30 times higher than those from narrowband (NB) LAE surveys but comparable to dust-corrected UV estimates, if nearly all the Ly α photons from these galaxies escape without dust absorption (Croft et al. 2016). They updated their measurements in Croft et al. (2018) using SDSS Data Release (DR) 12. After careful examination for possible contaminations and systematics, the corrected cross-correlation is \sim 50% lower than the DR10 result of Croft et al. (2016). They also performed cross-correlation of the Ly α emission and Ly α forest as complementary evidence, which presented no signal, and claimed that quasars would dominate the Ly α SB within 15 h^{-1} cMpc.

Inspired by the cross-correlation technique in Croft et al. (2016, 2018), we measure the Ly α SB on scales of several Mpc from quasars using the up-to-date LRG spectra and quasar catalog in SDSS DR16, much larger samples than those in Croft et al. (2018). In Section 2 we introduce the data samples used in this work. We compute the quasar–Ly α emission cross-correlation and obtain the projected SB profile in Section 3. In Section 4, Ly α forest–Ly α emission cross-correlation is carried out as a complementary measurement. In Section 5 we perform simple analysis on our results and investigate possible Ly α sources for our detected signals. Our methods to remove potential contamination are presented in Appendix A.

Throughout this paper, we adopt a spatially flat lambda cold dark matter (Λ CDM) cosmological model according to the Planck 2018 results (Planck Collaboration et al. 2020), with $H_0=100~h~{\rm km~s^{-1}~Mpc^{-1}}$ with $h=0.674,~\Omega_m=0.315,$ $\Omega_b h^2=0.0224,$ and $\Omega_c h^2=0.120.$ We use pMpc (physical megaparsecs) or pkpc (physical kiloparsecs) to denote physical distances and cMpc to denote comoving megaparsecs.

2. Data Samples

The data used in this study are selected from the final eBOSS data in SDSS DR16 (Ahumada et al. 2020), the fourth data release of the fourth phase of SDSS (SDSS-IV), which contains SDSS observations through 2018 August. As the largestvolume survey of the universe to date, eBOSS is designed to study the expansion and structure growth history of the universe and constrain the nature of dark energy by spectroscopic observation of galaxies and quasars. The spectrograph for SDSS-IV eBOSS covers a wavelength range of 3650–10400 Å, with a resolution of $\lambda/\Delta\lambda \sim 1500$ at 3800 Å and \sim 2500 at 9000 Å. There are 1000 fibers per 7 deg² plate, and each fiber has a diameter of 120 μ m, i.e., a 2" angle. There are two spectrographs, each collecting data from 500 fibers, roughly 450 dedicated to science targets and 50 to flux calibration and sky background subtraction. The eBOSS data from SDSS DR16 also include spectra obtained using the SDSS-I/II spectrographs covering 3800–9100 Å.

In this work, we correlate the residual flux in the galaxy spectra (after subtracting best-fit galaxy spectral templates)

with quasars and the $Ly\alpha$ forest to extract information on high-redshift $Ly\alpha$ emission imprinted in the galaxy fiber spectra. We describe the quasar catalog, the LRG spectra, and the $Ly\alpha$ forest samples used in this work.

2.1. Quasar Catalog

The SDSS DR16 quasar catalog (DR16Q; Lyke et al. 2020), the largest selection of spectroscopically confirmed quasars to date, contains 750,414 quasars in total, including 225,082 new quasars observed for the first time. DR16Q includes different redshift estimates generated by different methods, such as the SDSS spectroscopic pipeline, visual inspection, and principal component analysis (PCA). It also provides a "primary" redshift for each quasar, which is selected from, most preferably, the visual inspection redshift or, alternatively, the SDSS automated pipeline redshift. In this work we adopt the "primary" redshift and apply a redshift restriction of $2.0 \le z < 3.5$. This redshift cut was also adopted in Croft et al. (2016, 2018) due to the spectrograph cutoff for lowredshift Ly α emission and the limited number of observed quasars at higher redshifts. Further, we exclude quasars with redshift estimates of "catastrophic failures," if their PCA-based redshift estimates have a velocity difference of $|\Delta v|$ > 3000 km s⁻¹ from the "primary" redshift. We end up with 255,570 quasars in total, with a median redshift of 2.40.

2.2. LRG Spectra

For one of the main projects of the SDSS surveys, a large sample of LRGs have been observed spectroscopically to detect the baryon acoustic oscillation feature. BOSS was conducted during 2009-2014, producing two principal galaxy samples, LOWZ and CMASS (Reid et al. 2015). The BOSS LOWZ galaxy sample targeted the 343,160 low-redshift galaxy population spanning redshifts 0.15 < z < 0.43, to extend the SDSS-I/II Cut-I LRG sample (Eisenstein et al. 2001) by selecting galaxies of dimmer luminosity. The BOSS CMASS galaxy sample targeted 862,735 higher-redshift (0.43 < z < 0.75) galaxies. It used similar color-magnitude cuts to those utilized for the Cut-II LRGs from SDSS-I/II and the LRGs in 2SLAQ (Cannon et al. 2006), but with the galaxy selection toward bluer and fainter galaxies. Operated over 2014-2019, the eBOSS LRG sample (Ahumada et al. 2020) extended the high-redshift tail of the BOSS galaxies, with 298,762 LRGs covering a redshift range of 0.6 < z < 1.0.

We select 1,389,712 LRG spectra from the combination of the BOSS LOWZ sample, BOSS CMASS sample, and eBOSS LRG sample. These LRG spectra have been wavelength-calibrated, sky-subtracted, and flux-calibrated, and are the coadded ones of at least three individual exposures, with a uniform logarithmic wavelength grid spacing of $\Delta \log_{10} \lambda = 10^{-4}$ (about 69 km s $^{-1}$ per pixel). Each spectrum has an inverse variance per pixel to estimate the uncertainty, which incorporates photon noise, CCD read noise, and sky subtraction error. Bad pixels are flagged by pixel mask information, and we use ${\tt AND_MASK}$ provided by SDSS to rule out bad pixels in all exposures.

Each LRG spectrum has a best-fitting model spectrum obtained by performing rest-frame PCA using four eigenspectra as the basis (Bolton et al. 2012). A set of trial redshifts are explored by shifting the galaxy eigenbasis and modeling their minimum-chi-square linear combination. A quadratic

polynomial is added to fit some low-order calibration uncertainties, such as the Galactic extinction, intrinsic extinction, and residual spectrophotometric calibration errors. For each fiber, any objects along the corresponding line of sight that fall within the fiber aperture can have their emission imprinted in the spectrum. For example, the LRG fiber may capture the signal of diffuse $\text{Ly}\alpha$ emission originating from high-redshift galaxies and the IGM, and this is the signal we intend to extract in this work.

In the following analysis we only use the pixels from 3647 to 5470 Å in the observed frame, corresponding to Ly α emission in the redshift range 2.0 < z < 3.5.

2.3. Lya Forest

The Ly\$\alpha\$ forest samples\$^3 used in this work are selected from the "Ly\$\alpha\$ regions," \$\lambda_{RF} \in [1040, 1200] \text{ Å, of } 210,005 BOSS/ eBOSS quasar spectra ranging from \$z = 2.1\$ to \$z = 4\$ (du Mas des Bourboux et al. 2020), where \$\lambda_{RF}\$ represents the wavelength in the quasar's rest frame. Broad absorption line quasars, bad observations, and spectra whose Ly\$\alpha\$ regions have less than 50 pixels are all excluded. Then every three original pipeline spectral pixels (\$\Delta\$log\$_{10} \$\lambda \sim 10^{-4}\$) are rebinned (\$\Delta\$log\$_{10} \$\lambda \sim 3 \times 10^{-4}\$) for the purpose of measuring Ly\$\alpha\$ correlations.

For each spectral region the flux transmission fields are estimated by the ratio of the observed flux, f_q , to the mean expected flux, $\langle F_q \rangle$ (du Mas des Bourboux et al. 2020):

$$\delta_f(\lambda) = \frac{f_q}{\langle F_q \rangle} - 1. \tag{1}$$

The pipeline deals with $Ly\alpha$ forests with identified damped $Ly\alpha$ systems (DLAs) cautiously. Pixels where a DLA reduces the transmission by more than 20% are masked, and the absorption in the wings is corrected using a Voigt profile following the procedure described in Noterdaeme et al. (2012). We also mask ± 50 Å regions around the DLA positions predicted by Ho et al. (2021), to ensure that DLA contamination is removed. The number of remaining $Ly\alpha$ forest pixels is $\sim 3.4 \times 10^7$, with a median redshift of 2.41.

3. Quasar-Ly α Emission Cross-correlation

As the SDSS fiber would capture signals from high-redshift background sources, the LRG residual spectra, with the best-fit galaxy model spectra subtracted, may have Ly α emission from the high-redshift galaxies and IGM/CGM superposed. However, the signals are overwhelmed by noises in most cases. Cross-correlating the residual spectrum pixels with quasar positions is equivalent to stacking the Ly α signal in the quasar neighborhood. Suppressing the noise, the cross-correlation technique makes it possible to exceed current observation limits and detect diffuse Ly α emission with dimmer luminosities (Croft et al. 2016, 2018).

In this section we perform and analyze the quasar–Ly α cross-correlation using the quasar catalog and LRG spectra mentioned in Section 2. In Section 3.1 we describe the detailed measurement of the 2D cross-correlation as a function of the separations along and perpendicular to the line-of-sight direction. We measure the corresponding projected SB profile

in Section 3.2 and multipoles of the redshift-space two-point correlation function (2PCF) in Section 3.3.

3.1. Cross-correlation Transverse and Parallel to the Line of Sight

First we split the LRGs into 885 subsamples based on their angular positions, identified by the HEALPix (Górski et al. 2005) number with $N_{\rm side}=16$, which makes it convenient to search for neighboring quasars within a limited sky region. After obtaining a quasar–LRG spectrum pixel pair with an angular separation of θ , we can compute the line-of-sight separation r_{\parallel} and transverse separation r_{\perp} between these two objects:

$$r_{\parallel} = [D_C(z_{\text{Ly}\alpha}) - D_C(z_q)]\cos\frac{\theta}{2},\tag{2}$$

$$r_{\perp} = [D_M(z_{\text{Ly}\alpha}) + D_M(z_q)]\sin\frac{\theta}{2},\tag{3}$$

where D_C is the line-of-sight comoving distance as a function of redshift z, D_M is the transverse comoving distance as a function of redshift z, z_q is the quasar redshift, and $z_{\rm Ly\alpha}$ is the redshift of ${\rm Ly}\alpha$ emission converted from the wavelength of the LRG spectrum pixel, i.e., $z_{\rm Ly\alpha} = \lambda/\lambda_{\rm Ly\alpha} - 1$ with $\lambda_{\rm Ly\alpha} = 1215.67 {\rm \mathring{A}}$.

Following Croft et al. (2016), we estimate the quasar–Ly α emission SB cross-correlation, $\xi_{q\alpha}(r_{\perp}, r_{\parallel})$, by summing over all quasar–LRG spectrum pixel pairs separated by r_{\parallel} along the line-of-sight direction and by r_{\perp} along the transverse direction within a certain bin:

$$\xi_{q\alpha}(r_{\parallel}, r_{\perp}) = \frac{1}{\sum_{i=1}^{N(r)} w_{ri}} \sum_{i=1}^{N(r)} w_{ri} \Delta_{\mu, ri}, \tag{4}$$

where $N(\mathbf{r})$ is the number of LRG spectrum pixels within the separation bin centered at the position $\mathbf{r} = (r_{\perp}, r_{\parallel})$ and $\Delta_{\mu,ri} = \mu_{ri} - \langle \mu(z) \rangle$ denotes the fluctuation of Ly\alpha SB for the ith pixel in this bin. Here, μ_{ri} is the residual SB calculated by subtracting the best-fit galaxy model spectra from the observed LRG spectra and dividing the residuals by the angular area of the SDSS fiber, and $\langle \mu(z) \rangle$ is the average residual SB at each redshift (Figure 1), obtained by stacking the SB of all residual LRG spectra in the observed frame. The spectral interval $\Delta\log_{10}\lambda=10^{-4}$ (about 69 km s $^{-1}$ per pixel) in the SDSS spectra is kept when we compute $\langle \mu(z) \rangle$. The pixel weight ω_{ri} is the inverse variance of the flux, $1/\sigma_{ri}^2$, for valid pixels and zero for masked pixels. To avoid stray light contamination from quasars on the CCD, similar to Croft et al. (2016), we exclude any LRG spectrum once it is observed within five fibers or fewer away from a quasar fiber (i.e., $\Delta_{\text{fiber}} \leq 5$), as discussed in Appendix A.1. A more detailed analysis of the potential contamination in our measurement and the correction to possible systematics are discussed in Appendix A.

Note that the average residual SB shown in Figure 1 differs from that in Croft et al. (2016), mainly due to improved algorithms in flux calibration and extraction for DR16.⁴ Nevertheless, the strong features at the zero-redshift calcium H and K lines and mercury G line remain the largest excursions. This difference has little impact on the following

https://data.sdss.org/sas/dr16/eboss/lya/Delta_LYA/

⁴ https://www.sdss.org/dr16/spectro/pipeline/#ChangesforDR16

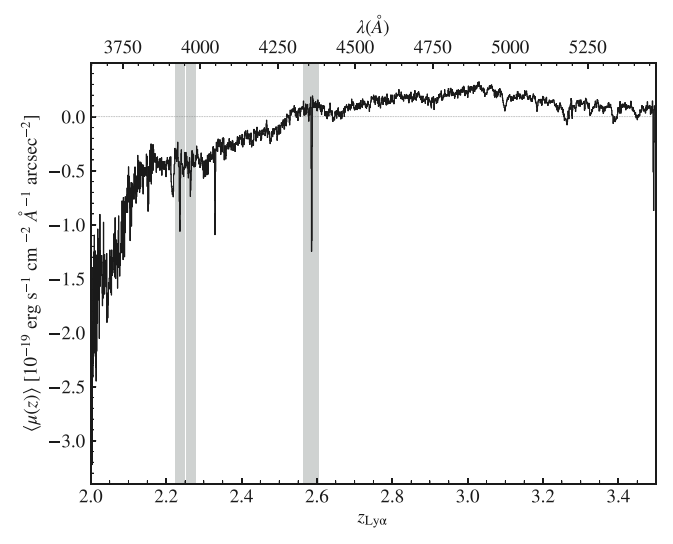


Figure 1. The average residual SB $\langle \mu(z) \rangle$, obtained by averaging all the individual residual spectra in the observed frame after subtraction of the best-fit galaxy model spectra from the LRG spectra. The gray regions, centered at 3934 Å and 3969 Å spanning 30 Å and at 4358 Å spanning 40 Å, are masked for zero-redshift Ca H and K lines and the strong mercury G line from streetlamps.

analysis, since the residual continuum contributes only to the statistical noise in the measurement, not to the signal. The feature around 4050 Å might be due to one of the sky emission lines, Hg I 4047 Å. We decide not to mask it, as we also do not specially deal with regions where other sky lines may reside. Since it is not the flux of $\langle \mu(z) \rangle$ itself but the fluctuation level Δ_{μ} relative to it that matters (see Equation (4)), this feature, shared by all individual residual spectra, will not affect our cross-correlation measurements.

We show the quasar-Ly α emission cross-correlation on a linear scale in Figure 2. The contours are somewhat stretched along the r_{\parallel} direction for r_{\perp} below a few h^{-1} Mpc. Croft et al. (2016) quantified the redshift-space anisotropies by assuming a linear ΛCDM correlation function shape distorted by a peculiar velocity model, which includes standard linear infall for largescale flows and a small-scale random velocity dispersion. In fact the elongation in the r_{\parallel} direction can be caused by a combination of multiple factors, including the intrinsic velocity dispersion of quasars in their host halos, the intrinsic velocity dispersion of the sources of Ly α emission, and quasar redshift uncertainties. The uncertainty in quasar redshifts primarily comes from systematic offsets between measured redshifts adopting different indicators, which can sometimes become large due to the complexity of physical processes related to broad emission lines. That makes it difficult to precisely and accurately disentangle a systemic redshift. For example, the variation of quasar redshift offsets between Z PCA (redshift estimated by PCA) and Z_MgII (redshift indicated by MgII emission lines) in DR16 can reach over $\pm 500 \text{ km s}^{-1}$ (Pâris et al. 2018; Lyke et al. 2020; Brodzeller & Dawson 2022), which corresponds to $\sim \pm 4.7 \ h^{-1}$ cMpc.

3.2. Projected Lya Emission SB

In this subsection, we measure the projected Ly α SB profile in a pseudo-NB by collapsing the 2D cross-correlation along the line-of-sight direction. There have been previous studies of

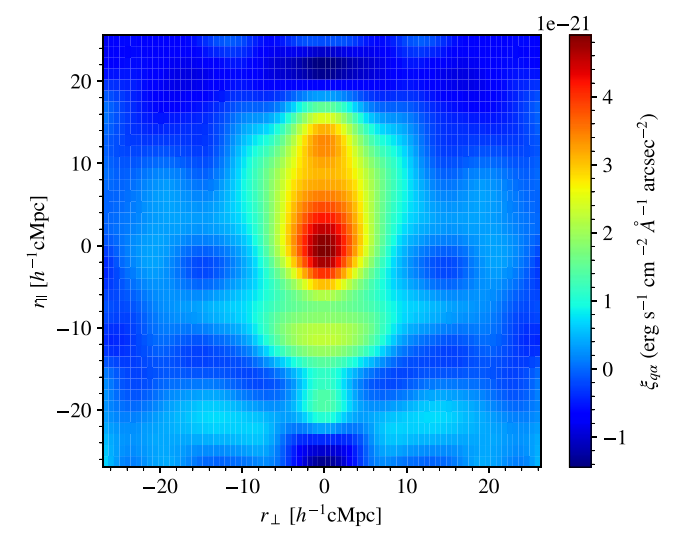


Figure 2. The quasar–Ly α emission cross-correlation as a function of r_{\perp} and r_{\parallel} . To reduce noise in the image, the data is smoothed with a 2D Gaussian kernel with a standard deviation of 4 h^{-1} cMpc. Potential light contamination is removed by a pixel veto. For display, the pattern is mirrored along $r_{\perp}=0$.

Ly α SB profiles around quasars. In order to compare them to our derived profile, we first summarize those observations.

Cai et al. (2019) studied quasar circumgalactic Ly α emission using KCWI observations of 16 ultraluminous Type I quasistellar objects (QSOs) at z=2.1-2.3. They integrated over a fixed velocity range of $\pm 1000~{\rm km~s}^{-1}$ around the centroid of Ly α nebular emission to calculate the SB. The median Ly α SB profile in their work can be described by the following power-law profile centered at the QSO at a projected radius r_{\perp} of 15–70 pkpc, which we denote as SB_C:

SB_C(
$$z \approx 2.3$$
) = 3.7 × 10⁻¹⁷ × (r_{\perp} /10 pkpc)^{-1.8}
× erg s⁻¹ cm⁻² arcsec⁻². (5)

Borisova et al. (2016) found large Ly α nebulae on a spatial extent of >100 pkpc from a MUSE snapshot survey on 17 radio-quiet QSOs at z>3.1. Twelve of them were selected specifically for their study from the catalog of Véron-Cetty & Véron (2010), as the brightest radio-quiet quasars known in the redshift range of z=3.0–3.3, and the other five at z=3.6–4.0 were selected originally for studying absorption line systems in quasar spectra. They fixed the width of their pseudo-NB images to the maximum spectral width of the Ly α nebulae, with a median of 43 Å. The median of their integrated SB profiles, denoted as SB_B here, can be described as

SB_B(
$$z \approx 3.1$$
) = $3.2 \times 10^{-17} \times (r_{\perp}/10 \text{ pkpc})^{-1.8}$
 $\times \text{erg}^{-1} \text{ cm}^{-2} \text{ arcsec}^{-2}$. (6)

Further, Croft et al. (2018) used a power law,

$$SB_{Croft}(z \approx 2.55) = 3.5 \times 10^{-19} \times (r_{\perp}/cMpc)^{-1.5} \times \text{erg s}^{-1} \text{ cm}^{-2} \text{ arcsec}^{-2},$$
 (7)

to follow the broad trend seen in the data.

If we make a simple correction for cosmological SB dimming to z = 2.40, the median redshift of our quasar sample, by scaling with a factor of $(1 + z)^4$, the above SB profiles

become

$$\begin{split} \mathrm{SB_C}(z \approx 2.40) &= 3.3 \times 10^{-17} \times (r_\perp/10 \ \mathrm{pkpc})^{-1.8} \\ &\times \mathrm{erg} \ \mathrm{s}^{-1} \ \mathrm{cm}^{-2} \, \mathrm{arcsec}^{-2} \,, \\ \mathrm{SB_B}(z \approx 2.40) &= 6.8 \times 10^{-17} \times (r_\perp/10 \ \mathrm{pkpc})^{-1.8} \\ &\times \mathrm{erg}^{-1} \ \mathrm{cm}^{-2} \, \mathrm{arcsec}^{-2} \,, \end{split} \tag{8}$$

and

$$SB_{Croft}(z \approx 2.40) = 4.16 \times 10^{-19} \times (r_{\perp}/cMpc)^{-1.5} \times erg s^{-1} cm^{-2} arcsec^{-2}$$
. (9)

To properly compare our measured SB with the SB of these previous works, we first collapse the 2D cross-correlation measurement in Section 3.1 along r_{\parallel} to obtain the SB as a function of r_{\perp} . We integrate the cross-correlation over a fixed line-of-sight window of ± 1000 km s⁻¹, corresponding to a window spanning ± 4 Å around $\lambda_{\rm Ly\alpha} \approx 1216$ Å in the z=2.40 quasar rest frame, or to a window of ± 9.37 h^{-1} cMpc around the quasar.

We use the jackknife method to compute the standard deviation of the obtained SB, by drawing a jackknife sample set from the 885 LRG subsamples and performing a cross-correlation with the quasar sample. The covariance matrix C_{ij} can be written as

$$C_{ij}(r_{\perp,i}, r_{\perp,j}) = \frac{n-1}{n}$$

$$\times \sum_{k=1}^{n} [SB_k(r_{\perp,i}) - \overline{SB}(r_{\perp,i})][SB_k(r_{\perp,j}) - \overline{SB}(r_{\perp,j})], \quad (10)$$

where $SB_k(r_{\perp,i})$ is the SB in bin *i* centered at the transverse separation $r_{\perp,i}$ for the jackknife sample k, $\overline{SB}(r_{\perp,i})$ denotes the SB measured from the full LRG data set, and the number of jackknife samples, n, is 885.

As shown in Figure 3, we have a detection of the SB profile at a projected radius r_{\perp} ranging from $\sim 0.1~h^{-1}\,\mathrm{cMpc}$ to $\sim 100~h^{-1}\,\mathrm{cMpc}$.

The SB profile within $r_{\perp} \leq 0.5 \, h^{-1}$ cMpc appears to be consistent with the observations of QSO nebulae on smaller scales in Cai et al. (2019) and Borisova et al. (2016), and on scales of 1 h^{-1} cMpc $\leq r_{\perp} \leq 10 \, h^{-1}$ cMpc our profile broadly agrees with the power-law fit in Croft et al. (2018).

3.3. Multipoles of the Redshift-space 2PCF

In addition to measuring the quasar–Ly α emission cross-correlation function (a.k.a. the 2PCF) in bins of r_{\perp} and r_{\parallel} , to better describe its shape, we further measure the cross-correlation in bins of s and μ , where s is the separation between quasars and Ly α pixels, i.e., $s = \sqrt{r_{\perp}^2 + r_{\parallel}^2}$, and μ is the cosine of the angle between s and the line-of-sight direction, $\mu = r_{\parallel}/s$.

The redshift-space 2PFC $\xi(s, \mu)$ can be expanded into multipoles, with the multipole moment ξ_{ℓ} calculated by Hamilton (1992):

$$\xi_l(s) = \frac{2l+1}{2} \int_{-1}^1 \xi(s, \mu) \mathcal{L}_{\ell}(\mu) d\mu, \tag{11}$$

where \mathcal{L}_{ℓ} is the ℓ th-order Legendre polynomial. In the linear regime (Kaiser 1987), there are three nonzero components of the redshift-space 2PCF—the monopole ξ_0 , the quadrupole ξ_2 ,

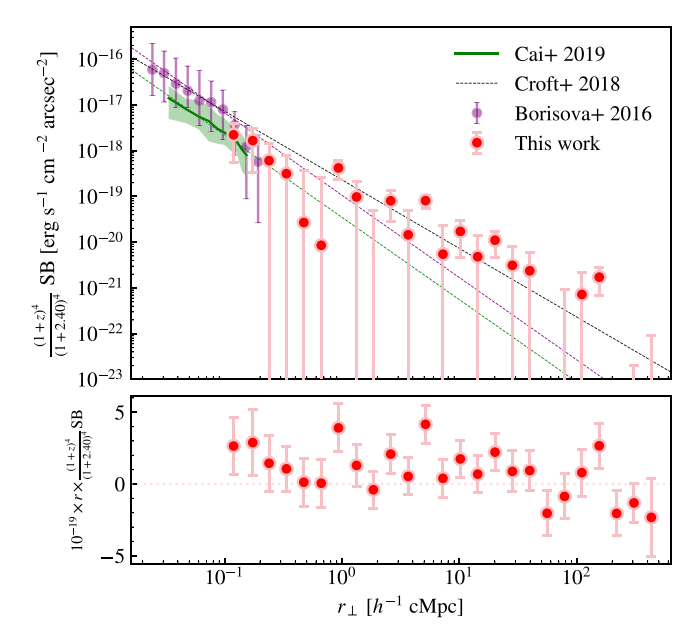


Figure 3. Projected Ly α SB profile (red points) around quasars obtained from our cross-correlation measurement. For comparison, the power-law fit (Equation (9)) from the IM result in Croft et al. (2018) is shown as a black dashed line. The SB profiles from observations of Ly α emission around quasars on smaller scales are shown as a green-shaded region (representing the range of 25th and 75th percentiles in Cai et al. 2019) and purple points (Borisova et al. 2016), with green and purple dashed lines denoting the power-law fit and extrapolation (Equation (8)). In the bottom panel, the measured SB is shown in linear scale.

and the hexadecapole ξ_4 :

$$\xi(s,\mu) = \sum_{\ell=0,2,4} \xi_{\ell}(s) \mathcal{L}_{\ell}(\mu). \tag{12}$$

At small transverse separations, however, the redshift-space 2PCF is affected by small-scale nonlinear effects, such as the finger-of-God effect, and also by the quasar redshift uncertainty in our cases. To reduce the small-scale contamination, we follow McCarthy et al. (2019) in adopting truncated forms of the multipoles by limiting the calculation to large transverse separations ($r_{\perp} > r_{\perp, \text{cut}}$):

$$\hat{\xi}_{\ell} = \frac{2\ell + 1}{2} \int_{-\mu_{\text{max}}}^{\mu_{\text{max}}} \xi(s, \mu) \mathcal{L}_{\ell}(\mu) d\mu, \tag{13}$$

where $\mu_{\text{max}} = \sqrt{1 - (r_{\perp,\text{cut}}/s)^2}$. The transformation between $\boldsymbol{\xi} = (\xi_0, \, \xi_2, \, \xi_4)^T$ and $\hat{\boldsymbol{\xi}} = (\hat{\xi}_0, \, \hat{\xi}_2, \, \hat{\xi}_4)^T$ can be described using a 3×3 matrix \boldsymbol{R} :

$$\hat{\boldsymbol{\xi}} = \boldsymbol{R}\boldsymbol{\xi},\tag{14}$$

where

$$R_{\ell k} = \frac{2\ell + 1}{2} \int_{-\mu_{\text{max}}}^{\mu_{\text{max}}} \mathcal{L}_{\ell}(\mu) \mathcal{L}_{k}(\mu) d\mu \quad \text{for } \ell, k = 0, 2, 4.$$
(15)

In our measurement we set $r_{\perp,\mathrm{cut}} = 4 \ h^{-1} \,\mathrm{cMpc}$ to ensure that the bulk of small-scale contamination is excluded. The multipole measurements will be presented along with the modeling results.

3.4. Modeling the Quasar-Ly\alpha Emission Cross-correlation

In Croft et al. (2016), the amplitude of the measured quasar— Ly α emission cross-correlation, if modeled by relating Ly α emission to star-forming galaxies, would imply a value of Ly α emissivity comparable to that inferred from the cosmic SFRD without dust correction, appearing too high compared with predictions from the Ly α luminosity functions (LFs) of Ly α emitting galaxies. In Croft et al. (2018), with the correction to the systematic effect from quasar clustering and the complementary measurement of the Ly α forest-Ly α emission crosscorrelation, the detected Ly α emission was found to be explained by Ly α emission associated with quasars based on populating a large hydrodynamic cosmological simulation. In this subsection we will revisit both scenarios by constructing a simple analytic model to describe the measured Ly α intensity, and argue that the observed Ly α emission cannot be only contributed by quasars. The simple model can also be applied to Ly α forest-Ly α emission cross-correlation, and our corresponding prediction and detailed analysis are presented in Section 4.

We assume that the Ly α emission from sources clustered with quasars contributes the bulk of the detected signals on large scales, while on small scales the Ly α photons are associated with the central quasar count. Supposing that $\langle \mu_{\alpha} \rangle$ is the mean SB of Ly α emission, and b_q and b_{α} are the linear bias factors of quasars and Ly α sources, respectively, in the linear regime the nonvanishing multipoles of the redshift-space quasar-Ly α emission cross-correlation are given by

$$\xi_{0}(s) = b_{q}b_{\alpha}\langle\mu_{\alpha}\rangle f_{\beta,0}\,\xi_{mm}(r),$$

$$\xi_{2}(s) = b_{q}b_{\alpha}\langle\mu_{\alpha}\rangle f_{\beta,2}\,[\xi_{mm}(r) - \bar{\xi}_{mm}(r)],$$

$$\xi_{4}(s) = b_{q}b_{\alpha}\langle\mu_{\alpha}\rangle f_{\beta,4}\,\bigg[\,\xi_{mm}(r) + \frac{5}{2}\bar{\xi}_{mm}(r) - \frac{7}{2}\bar{\xi}_{mm}(r)\,\bigg],$$
(16)

where (e.g., Percival & White 2009)

$$f_{\beta,0} = 1 + \frac{1}{3}(\beta_q + \beta_\alpha) + \frac{1}{5}\beta_q\beta_\alpha,$$

$$f_{\beta,2} = \frac{2}{3}(\beta_q + \beta_\alpha) + \frac{4}{7}\beta_q\beta_\alpha,$$

$$f_{\beta,4} = \frac{8}{35}\beta_q\beta_\alpha,$$
(17)

and (e.g., Hawkins et al. 2003)

$$\overline{\xi}(r) = \frac{3}{r^3} \int_0^r \xi(r') r'^2 dr',$$

$$\overline{\xi}(r) = \frac{5}{r^5} \int_0^r \xi(r') r'^4 dr'.$$
(18)

Note that r is the distance in real space and s denotes the distance in redshift space and in the above expressions r = s. Then the model for the truncated 2PCF $\hat{\xi}$ can be obtained according to Equations (14) and (15).

The redshift-space distortion parameter β_q for quasars depicts the redshift-space anisotropy caused by peculiar velocity, $\beta_q = \Omega_m^{0.55}(z=2.4)/b_q$. We fix $b_q = 3.64$ according to Font-Ribera et al. (2013). The redshift-space distortion parameter β_α for Ly α emission is similarly defined. We set $b_\alpha = b_q$ for the case where the main contributors to Ly α emission are clustered quasars and $b_\alpha = 3$ for the case where Ly α emission is dominated by contributions from star-forming

galaxies. A value of 3 appears to be a good estimate of the luminosity-weighted bias b_{α} for star-forming galaxies. Following Croft et al. (2016), we find that b_{α} is within \sim 5% of 3 with different low halo mass cuts and different prescriptions of the stellar mass-halo mass relation at $z\sim$ 2.4 (e.g., Moster et al. 2010, 2013; Behroozi et al. 2019). In both scenarios we leave β_{α} and $\langle \mu_{\alpha} \rangle$ as free parameters to be fitted. We note that β_{α} can potentially include additional effects other than the Kaiser effect, such as Ly α radiative transfer on clustering (Zheng et al. 2011a).

We also model the Ly α SB profile. As discussed in Section 3.2, previous observations indicate that the small-scale SB profile can be well described by a power law with an index of -1.8. We therefore decompose the full SB profile into two components: a one-halo term SB_{1h} dominated by Ly α emission associated with the central quasars and a two-halo term SB_{2h} dominated by the clustered Ly α sources,

$$\begin{split} \mathrm{SB}_{1\mathrm{h}} &= \mathrm{SB}_{0} \left(\frac{r_{\perp}}{1h^{-1} \, \mathrm{cMpc}} \right)^{-1.8}, \\ \mathrm{SB}_{2\mathrm{h}} &= \frac{\rho_{\mathrm{Ly}\alpha}}{4\pi (1+z)^{2}} \int_{\pi_{\mathrm{min}}}^{\pi_{\mathrm{max}}} \xi(r_{\perp}, \, r_{\parallel}) dr_{\parallel} \\ &= \frac{\rho_{\mathrm{Ly}\alpha}}{4\pi (1+z)^{2}} b_{q} b_{\alpha} (f_{\beta,0} w_{p,0} + f_{\beta,2} w_{p,2} + f_{\beta,4} w_{p,4}). \end{split} \tag{19}$$

Here ξ is the linear correlation function between quasars and Ly α emission sources (quasars or star-forming galaxies) in redshift space, $\rho_{\rm Ly}\alpha=4\pi\langle\mu_\alpha\rangle[H(z)/c]\lambda_\alpha(1+z)^2$ is the comoving Ly α luminosity density (Croft et al. 2016), and $\pi_{\rm max}$ and $\pi_{\rm min}$ correspond to $\pm 9.37~h^{-1}$ cMpc, the width of the pseudo-NB used in Section 3.2. The projected cross-correlation function is put in the form of the projected multipoles, which are calculated as

$$\begin{split} w_{p,0}(r_{\perp}) &= \int_{\pi_{\min}}^{\pi_{\max}} \; \xi_{mm}(r) \mathcal{L}_{0}(\mu) dr_{\parallel}, \\ w_{p,2}(r_{\perp}) &= \int_{\pi_{\min}}^{\pi_{\max}} \; [\xi_{mm}(r) - \bar{\xi}_{mm}(r)] \mathcal{L}_{2}(\mu) dr_{\parallel}, \\ w_{p,4}(r_{\perp}) &= \int_{\pi_{\min}}^{\pi_{\max}} \; \left[\xi_{mm}(r) + \frac{5}{2} \bar{\xi}_{mm}(r) - \frac{7}{2} \bar{\xi}_{mm}(r) \right] \mathcal{L}_{4}(\mu) dr_{\parallel}, \end{split}$$

$$(20)$$

with
$$r = \sqrt{r_{\perp}^2 + r_{\parallel}^2}$$
 and $\mu = r_{\parallel}/r$.

With three free parameters (SB₀, β_{α} , and $\langle \mu_{\alpha} \rangle$), we perform a joint fit to the three (large-scale) multipoles and the projected SB profile, assuming that the Ly α sources in the model are mainly star-forming galaxies and quasars, as respectively discussed in Sections 3.4.1 and 3.4.2.

3.4.1. Star-forming Galaxies as Ly\alpha Sources

In the case where Ly α emission is dominated by the contribution from galaxies, we fix $b_{\alpha}=3$. The best-fit results for the multipoles and the SB profile are shown in Figures 4 and 5. Given the uncertainties in the measurements, the model provides a reasonable fit and shows broad agreement with the trend in the data. The middle panel of Figure 6 shows a reconstructed 2D image of the redshift-space linear cross-correlation function from the best-fit model. If it is subtracted from the measurement (left panel), the residual (right panel) is dominated by the small-scale clustering that we do not model.

The constraints on the three parameters are presented in Figure 7. The parameter representing the amplitude of the

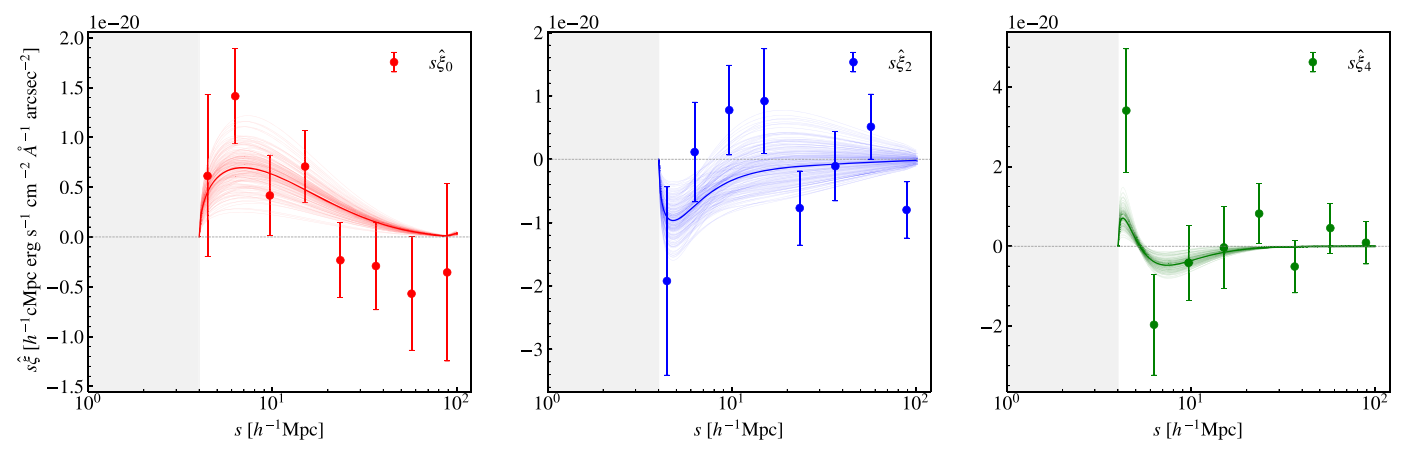


Figure 4. Modified monopole, quadrupole, and hexadecapole of the quasar— $Ly\alpha$ emission cross-correlation (see Equation (13)) and their fitting results based on the galaxy-dominated model (see Section 3.4.1). The points represent our measurements with jackknife error bars. The solid curves denote the modeled modified multipoles with parameters randomly drawn from their posterior probability distributions, among which the thickest ones correspond to the best fits. The modified multipoles remove any information within $r < r_{\perp, cut}$, i.e., the gray-shaded regions, to avoid small-scale contamination.

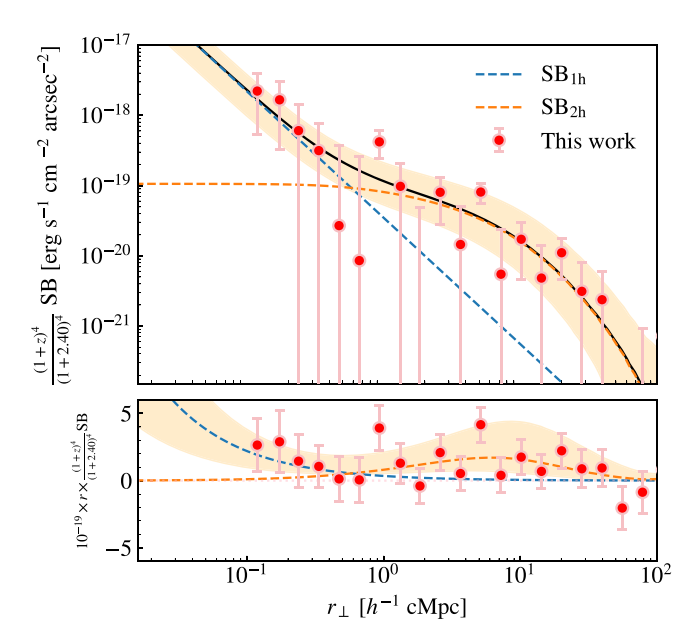


Figure 5. Ly α SB profile. The data points are from integrating the measured quasar–Ly α emission cross-correlation function along the line of sight, and the solid curve is the best-fit SB profile for the galaxy-dominated model depicted in Section 3.4.1. The dashed lines denote the best-fit one-halo and two-halo terms, and the shaded region represents the $\pm 1\sigma$ range. In the bottom panel, a linear scale is used on the *y*-axis.

one-halo term is loosely constrained, $SB_0=3.49^{+2.27}_{-2.02}\times 10^{-20}\,\mathrm{erg}\,\mathrm{s}^{-1}\,\mathrm{cm}^{-2}\,\mathrm{arcsec}^{-2}$. The parameter $\langle\mu_{\alpha}\rangle$, proportional to the comoving Ly\$\alpha\$ emissivity or luminosity density, is constrained at the 2σ level, $\langle\mu_{\alpha}\rangle=1.13^{+0.57}_{-0.53}\times 10^{-21}\,\mathrm{erg}\,\mathrm{s}^{-1}\,\mathrm{cm}^{-2}\,\mathring{\mathrm{A}}^{-1}\,\mathrm{arcsec}^{-2}$. The redshift-space distortion parameter has a high probability density of being negative but with a tail toward positive values, $\beta_{\alpha}=0.07^{+1.65}_{-0.73}$. Given its uncertainty, the value is consistent with that from the Kaiser effect, $\Omega_m(z=2.4)^{0.55}/b_{\alpha}\simeq 0.32$, and we are not able to tell whether there is any other effect (e.g., from radiative transfer; Zheng et al. 2011a).

We note that fitting the clustering measurements leads to an anticorrelation between $\langle \mu_{\alpha} \rangle$ and β_{α} (Equations (16) and (17); Figure 7). If β_{α} is restricted to the formal value of \sim 0.32 from

the Kaiser effect, the constraints on $\langle \mu_{\alpha} \rangle$ become $1.09^{+0.25}_{-0.24} \times 10^{-21}\,\mathrm{erg}\;\mathrm{s}^{-1}\,\mathrm{cm}^{-2}\,\mathring{\mathrm{A}}^{-1}\,\mathrm{arcsec}^{-2},$ a nearly 4σ detection. If we set the upper limit of β_{α} to 0.32 to allow room for the radiative transfer effect (e.g., Zheng et al. 2011a), the constraints change to $\langle \mu_{\alpha} \rangle = 1.44^{+0.45}_{-0.38} \times 10^{-21}\,\mathrm{erg}\;\mathrm{s}^{-1}\,\mathrm{cm}^{-2}\,\mathring{\mathrm{A}}^{-1}\,\mathrm{arcsec}^{-2}.$ In the following discussions, to be conservative, we take the $\langle \mu_{\alpha} \rangle$ constraints without these restrictions.

The constrained $\langle \mu_{\alpha} \rangle$ corresponds to a comoving Ly α luminosity density of $\rho_{\rm Ly\alpha}=6.6^{+3.3}_{-3.1}\times10^{40}\,{\rm erg~s^{-1}\,cMpc^{-3}}.$ This value is about 3.6 times lower than that in Croft et al. (2016) and \sim 2.2 times lower than that in Croft et al. (2018). With the lower amplitude, the fractional uncertainty is larger. The comparison is shown in Figure 8. We also show the Ly α luminosity densities at different redshifts calculated by integrating the Ly α LFs of LAEs down to low luminosity. For example, the LFs in Ouchi et al. (2008, 2010) were integrated down to $L_{{\rm Ly}\alpha}=0$ with the best-fit Schechter parameters for $z=3.1,\ 3.7,\ 5,\ 7,\ {\rm and}\ 6.6;$ those in Drake et al. (2017a), down to $\log[L_{\rm Ly\alpha}/({\rm erg~s^{-1}})] = 41.0$; and those in Sobral et al. (2018), down to $1.75 \times 10^{41} {\rm erg~s^{-1}}$. These quoted Ly α luminosity densities were inferred without separating the contribution of potential active galactic nuclei (AGNs) except at the very luminous end (see Wold et al. 2017 for a two-component fit). The luminous end is usually excluded in parameterized fits to Ly α LFs, but it does not contribute much to the total Ly α luminosity density due to its rather low number density. The quoted LAE Ly α luminosity densities in Figure 8 should have included the potential contribution of relatively faint AGNs (with AGNs detected in X-ray and radio contributing at a level of a few percent; Sobral et al. 2018). At $z \sim 2.4$, our inferred Ly α luminosity density is about one order of magnitude higher than that inferred from the LAE LF, although they can be consistent within the uncertainty.

We further show the H α -converted Ly α luminosity density as derived in Wold et al. (2017), which was obtained by scaling the H α luminosity density measured in HiZELS (Sobral et al. 2013) with an escape fraction of 5% and a correction of about 10% (15%) for AGN contribution at z < 1 (z > 1). The cosmic Ly α luminosity density measured by Chiang et al. (2019) through broadband IM is also shown, which probes the total background including low-SB emission by spatially cross-correlating

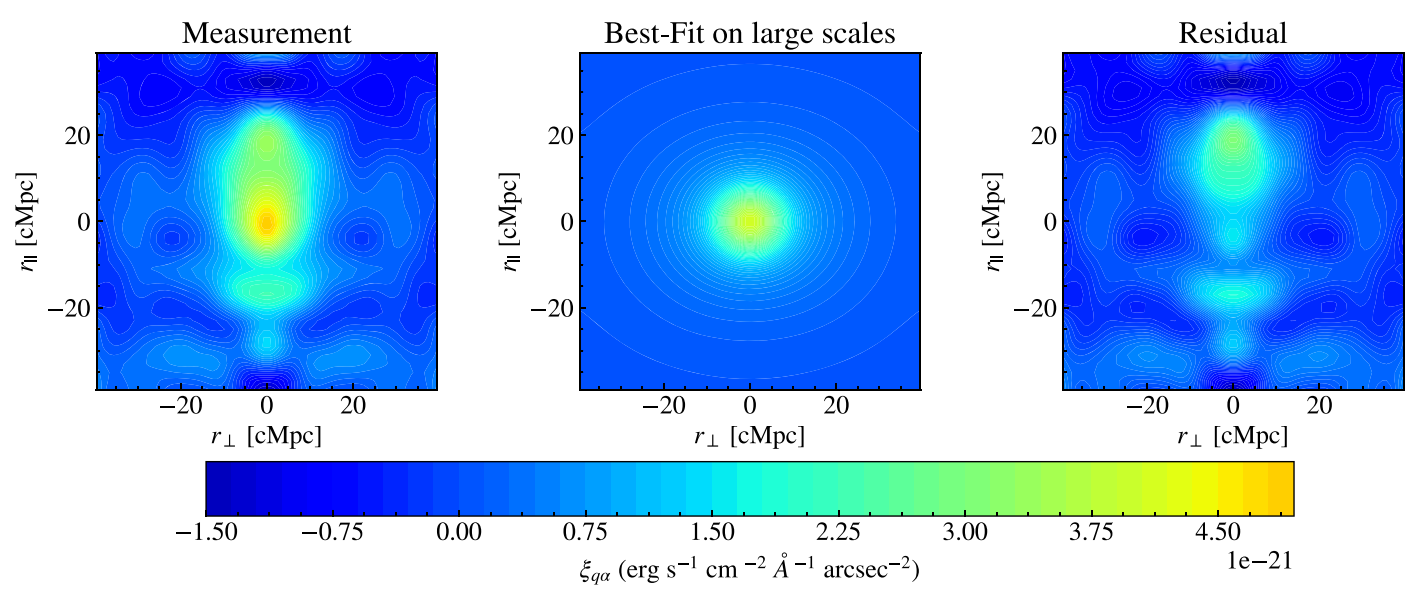


Figure 6. The measured (left panel), best-fit (middle panel), and residual (right panel) quasar— $Ly\alpha$ emission cross-correlation as a function of r_{\parallel} and r_{\perp} . The model fit is only to large-scale signals by using the modified multipoles (Equation (13)). The best-fit pattern shown here is reconstructed from the corresponding multipoles (Equation (16)) with the best-fit parameters. The residual is obtained by subtracting the best-fit model from the measurement, with elongated distortion along the r_{\parallel} direction on small scales, and small-scale anisotropy not included in our model. All the three images are smoothed using a 2D Gaussian kernel with a standard deviation of 4 h^{-1} cMpc.

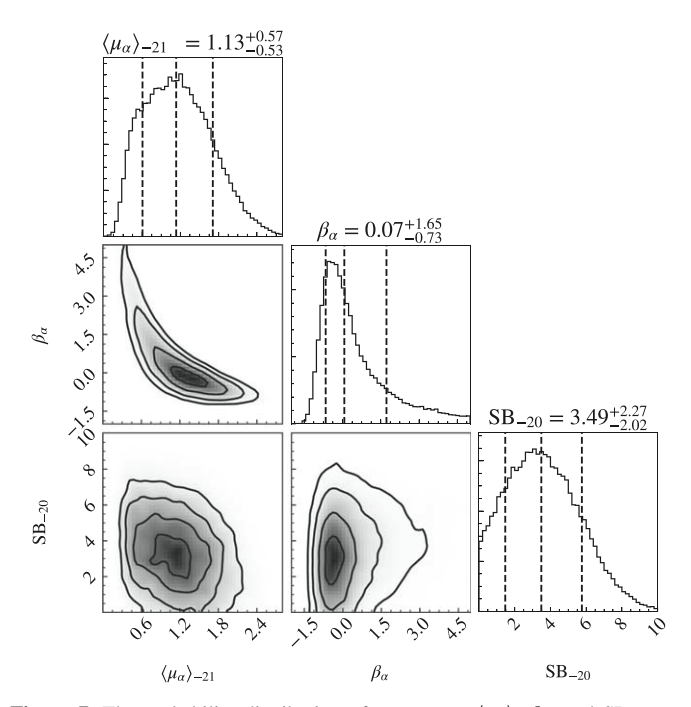


Figure 7. The probability distribution of parameters $\langle \mu_{\alpha} \rangle$, β_{α} , and SB₀ as a result of the joint fit to the modified multipoles and SB profile of the quasar–Ly α emission cross-correlation, with an assumption that star-forming galaxies dominate the large-scale Ly α emission and thus $b_{\alpha}=3$. The parameter $\langle \mu_{\alpha} \rangle_{-21}$ is $\langle \mu_{\alpha} \rangle$ in units of $10^{-21}\,\mathrm{erg}\,\mathrm{s}^{-1}\,\mathrm{cm}^{-2}\,\mathrm{Å}^{-1}\,\mathrm{arcsec}^{-2}$, and SB₋₂₀ is SB₀ in units of $10^{-20}\,\mathrm{erg}\,\mathrm{s}^{-1}\,\mathrm{cm}^{-2}\,\mathrm{arcsec}^{-2}$. The dashed lines in the histograms denote the 16th, 50th, and 84th percentiles of the marginalized distributions.

photons in far-UV and near-UV bands with spectroscopic objects. They claimed that the cosmic $Ly\alpha$ luminosity density they derived is consistent with cosmic star formation with an effective escape fraction of 10% assuming that all of the $Ly\alpha$ photons originate from star formation. Combining our measurement with the results of Chiang et al. (2019), it appears that the cosmic $Ly\alpha$ luminosity density grows with redshift over

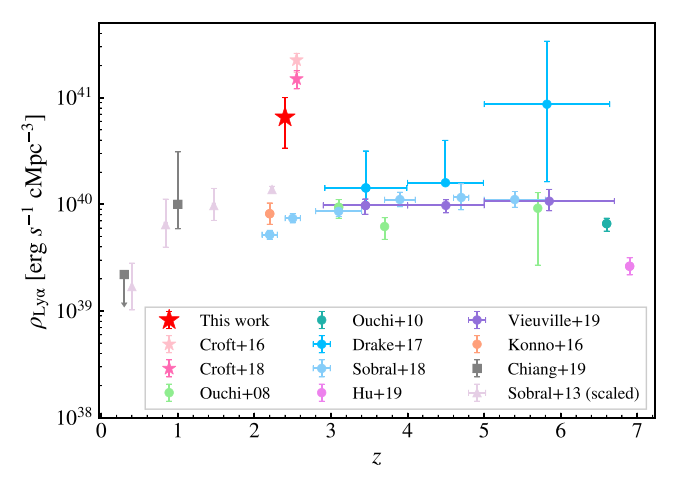


Figure 8. Ly α luminosity density $\rho_{\rm Ly}\alpha$. The red star shows the value inferred from our quasar–Ly α emission measurement, assuming that the detected Ly α emission is due to star-forming galaxies with a typical luminosity-weighted bias of $b_{\alpha}=3$. As a comparison, we also show the values with previous IM measurements (Croft et al. 2016, 2018; Chiang et al. 2019) and those from integrating the Ly α LFs of LAEs (Ouchi et al. 2008, 2010; Drake et al. 2017a; Sobral et al. 2018; de La Vieuville et al. 2019; Hu et al. 2019) and scaling H α luminosities with an escape fraction of 5% (Sobral et al. 2013; Wold et al. 2017).

 $0 \lesssim z \lesssim 2.5$, and more data points at different redshifts are expected to confirm this trend.

If we assume that all the Ly α emission originates from star formation, we can convert our inferred Ly α luminosity density to an SFRD, by using a simple conversion (Kennicutt 1998),

$$\rho_{\rm SFR}/(M_{\odot} \, {\rm yr^{-1} \, cMpc^{-3}}) = \frac{\rho_{\rm Ly\alpha}/({\rm erg \ s^{-1} \, cMpc^{-3}})}{1.1 \times 10^{42} ({\rm erg \ s^{-1}})/(M_{\odot} \, {\rm yr^{-1}})}. \tag{21}$$

This gives $\rho_{\rm SFR} = 0.06 \pm 0.03~M_{\odot}~{\rm yr}^{-1}~{\rm cMpc}^{-3}$, higher than that from integrating LAE LFs, as shown in Figure 9. The value is on the low end of the cosmic SFRD based on UV and

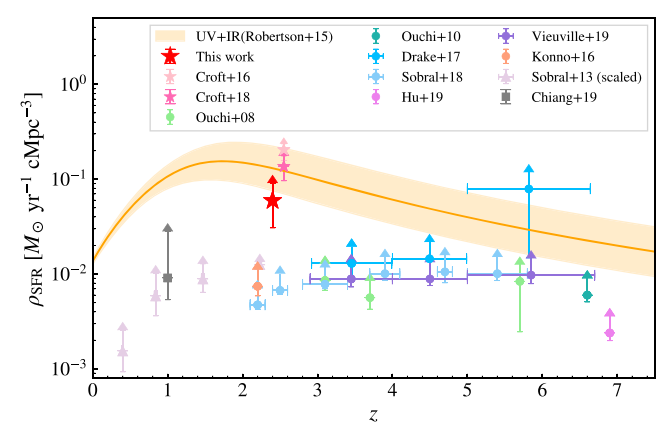


Figure 9. Same as Figure 8 but the $Ly\alpha$ luminosity density $\rho_{Ly\alpha}$ is converted to SFRD ρ_{SFR} under the assumption that $Ly\alpha$ emission is purely caused by star formation. Given the effect of dust extinction and the $Ly\alpha$ escape fraction, these $Ly\alpha$ -converted ρ_{SFR} values should be considered as lower limits of the intrinsic star formation. The orange-shaded region represents the parameterized model for the evolving SFRD in Robertson et al. (2015), based on IR and UV observations.

infrared (IR) observations (e.g., Robertson et al. 2015). However, we emphasize that the Ly α -converted ρ_{SFR} in this case should be treated as a lower limit for estimates of the intrinsic star formation, since no correction is applied to account for dust extinction and the Ly α escape fraction. The comparison in Figure 9 is simply to highlight the high amplitude of Ly α emission inferred from the quasar–Ly α emission cross-correlation.

3.4.2. Quasars as Ly\alpha Sources

In the case where $\mathrm{Ly}\alpha$ emission is dominated by the contribution from quasars, we make a simple assumption that the quasars involved are almost the same, with a typical $\mathrm{Ly}\alpha$ luminosity $L_{q,\alpha}$ and a comoving number density n_q , so that $\rho_{\mathrm{Ly}\alpha} = L_{\alpha,q} n_q$.

We calculate n_q by integrating the luminosity evolution and density evolution model (Ross et al. 2013) of the optical quasar LF (QLF), fitted using data from SDSS-III DR9 and allowing luminosity and density to evolve independently. The QLF gives the number density of quasars per unit magnitude, and its integration over the magnitude range of $M_i[z=2]=-30$ to $M_i[z=2]=-18$ yields $n_q\approx 1.34\times 10^{-4}~h^3\,{\rm Mpc}^{-3}$.

With the analytical model in this quasar-dominant scenario, we jointly fit both the measured cross-correlation multipoles and the SB profile, where b_{α} is fixed to b_q and $\rho_{\mathrm{Ly}\alpha}$ is interpreted to be $L_{\alpha,q}n_q$, leaving $L_{q,\alpha}$, β_{α} , and SB₀ as free parameters. Our joint fitting result, presented in Figure 10, indicates that the required quasar $\mathrm{Ly}\alpha$ luminosity under the above assumption should be $\log[L_{q,\alpha}/(\mathrm{erg}\ \mathrm{s}^{-1})] = 45.12^{+0.18}_{-0.27}$. The best-fit value is even brighter than those of some ultraluminous quasars usually targeted to search for enormous nebulae (e.g., $\sim 10^{43} - \lesssim 10^{45}\ \mathrm{erg}\ \mathrm{s}^{-1}$ in Cai et al. 2018). Such a high $\mathrm{Ly}\alpha$ luminosity per quasar makes the quasar-dominated model unlikely to work.

Our modeling result appears to be inconsistent with the quasar-dominated model in Croft et al. (2018). In their model, the Ly α SB profile on scales above $\sim 1 \, h^{-1}$ Mpc is well reproduced (see their Figure 10). Ly α emission in their model is presented as Ly α SB as a function of gas density and distance from the quasar, while the total Ly α luminosity per

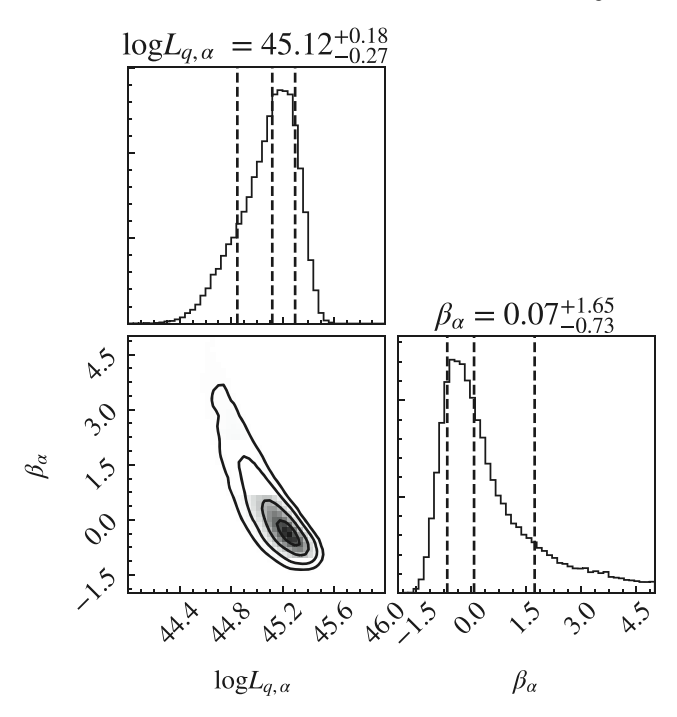


Figure 10. The probability distribution of $L_{q,\alpha}$ and β_{α} from the joint fit to the multipoles and SB profiles from the measured quasar–Ly α emission cross-correlation. The mean quasar Ly α luminosity $L_{q,\alpha}$ is in units of ergs per second. Note that there are actually three parameters, $L_{q,\alpha}$, β_{α} , and SB₀, in the model, but here we focus on the constraints on $L_{q,\alpha}$ and β_{α} . See the text for details.

quasar is not given. The luminosity, however, can be dominated on scales $\lesssim 1\ h^{-1}$ Mpc, which is not shown in their figure. Fortunately, panel (b) in their Figure 8 ("Model Q") enables an estimation of the mean quasar Ly α luminosity (R. Croft 2022, private communication). With a mean Ly α SB $\langle \mu_{\alpha} \rangle = 7.0 \times 10^{-22}\ {\rm erg\ s^{-1}\ cm^{-2}\ \mathring{A}^{-1}\ arcsec^{-2}}$ (their Section 5.1) from a slice with a thickness of $40\ h^{-1}$ Mpc (corresponding to the observed spread of $\sim 29\ \mathring{A}$ in Ly α emission) and a side length of $400\ h^{-1}$ Mpc ($\sim 2.04 \times 10^4\ arcsec$ at $z \sim 2.5$), we obtain a total Ly α luminosity in the slice of $\sim 4.0 \times 10^{47}\ {\rm erg\ s^{-1}}$. As there are about 100 quasars in the slice, the average Ly α luminosity in "Model Q" of Croft et al. (2018) is $\sim 4.0 \times 10^{45}\ {\rm erg\ s^{-1}}$, which agrees well with our result here.

In conclusion, the modeling results from our analytical models rule out the quasar-dominated scenario. For the galaxy-dominated scenario, however, both our measurement and that in Croft et al. (2018) imply that the detected Ly α signals cannot be explained simply by emission from currently observed LAEs. There must be additional Ly α -emitting sources other than these LAEs. We will explore the possibilities in Section 5 after presenting the Ly α forest–Ly α emission cross-correlation results in Section 4.

4. Ly α Forest-Ly α Emission Cross-correlation

The Ly α forest, as a probe of the cosmic density field, can be used as an alternative tracer more space-filling than quasars to detect diffuse Ly α emission on cosmological scales. The Ly α forest–Ly α emission cross-correlation can provide additional information for understanding the origin of the Ly α emission.

Following Croft et al. (2018), we measure the Ly α forest–Ly α emission cross-correlation in a way similar to that for the

quasar-Ly α emission cross-correlation:

$$\xi_{f\alpha}(r,\,\mu) = \frac{1}{\sum_{i=1}^{N(r)} w_{ri,\alpha} w_{ri,f}} \sum_{i=1}^{N(r)} w_{ri,\alpha} w_{ri,f} \Delta_{\mu,ri} \delta_{f,ri}, \qquad (22)$$

where $N(\mathbf{r})$ is the number of Ly α forest-Ly α emission pixel pairs within the bin centered at the separation $\mathbf{r}=(r,\mu)$. $\Delta_{\mu,ri}$ is the fluctuation of Ly α emission SB (from the residual LRG spectra) for the *i*th pixel pair in this bin, and $\delta_{f,ri}$ is the flux transmission field of the Ly α forest in the quasar spectra. The weights $w_{ri,\alpha}$ of the Ly α emission pixels are the same as in Equation (4), and the weights for the Ly α forest pixels $w_{ri,f}=1/\sigma_{ri,f}^2$, where $\sigma_{ri,f}^2$ is the pixel variance due to instrumental noise and large-scale structures, with the latter accounting for the intrinsic variance of the flux transmission field.

Likewise, we can decompose the 2D Ly α forest–Ly α emission cross-correlation into monopole, quadrupole, and hexadecapole moments. To avoid spurious correlation induced by same-half-plate pixel pairs, we only use pixel pairs residing on different half-plates and reject signals within $|r_{\parallel,\text{cut}}|=4$ cMpc, as discussed in Appendix A.2. Similar to what we do with the quasar–Ly α emission cross-correlation, we define the modified multipoles of the Ly α forest–Ly α emission cross-correlation as

$$\hat{\xi}_{f\alpha,\ell}(s) = \frac{2\ell+1}{2} \left(\int_{-1}^{-\mu_{\min}} \xi_{f\alpha}(s,\mu) \mathcal{L}_{\ell}(\mu) d\mu + \int_{\mu_{\min}}^{1} \xi_{f\alpha}(s,\mu) \mathcal{L}_{\ell}(\mu) d\mu \right), \tag{23}$$

where $\mu_{\min} = |r_{\parallel, \text{cut}}|/s$. As in Equation (15), the original and modified multipoles are connected through $\hat{\xi}_{f\alpha} = \mathbf{R}'\xi_{f\alpha}$, where the element of the transformation matrix \mathbf{R}' takes the form

$$R'_{\ell k} = 7 \frac{2\ell + 1}{2} \left(\int_{-1}^{-\mu_{\min}} \mathcal{L}_{\ell}(\mu) \mathcal{L}_{k}(\mu) d\mu + \int_{\mu_{\min}}^{1} \mathcal{L}_{\ell}(\mu) \mathcal{L}_{k}(\mu) d\mu \right), \tag{24}$$

with ℓ , k = 0, 2, or 4.

The analytical model for the Ly\$\alpha\$ forest-Ly\$\alpha\$ emission cross-correlation is similar to the one for the quasar-Ly\$\alpha\$ emission cross-correlation, and we only need to replace b_q and β_q in Equations (16) and (17) with b_f and β_f , respectively. Here b_f is the Ly\$\alpha\$ forest transmission bias, evolving with redshift as $b_f(z) = b_f(z_{\rm ref})[(1+z)/(1+z_{\rm ref})]^{\gamma_a}$ with $\gamma_\alpha = 2.9$, and β_f is the redshift distortion parameter for the Ly\$\alpha\$ forest, \$\beta_f = fb_\eta/b_f\$, where \$f\$ is the linear growth rate of structure and b_η is the velocity bias of the Ly\$\alpha\$ forest (e.g., Seljak 2012; Blomqvist et al. 2019). We fix $b_\eta = -0.225$ and $\beta_f = 1.95$ at a reference redshift of $z_{\rm ref} = 2.34$ according to the quasar-Ly\$\alpha\$ forest cross-correlation result in du Mas des Bourboux et al. (2020), yielding $b_f = -0.119$ at z = 2.41.

Given the small transmission bias b_f of the Ly α forest, the expected Ly α forest-Ly α emission cross-correlation level at $\sim 10~h^{-1}$ cMpc is $\sim 5\%$ of the quasar-Ly α emission cross-correlation. The subsequent low signal-to-noise ratio would lead to weak parameter constraints from fitting the Ly α forest-Ly α emission cross-correlation measurements. Instead we choose to compare the measurements with the predictions

from the model adopting the best-fit parameters, β_{α} and $\langle \mu_{\alpha} \rangle$, from modeling the quasar–Ly α emission correlation (Section 3.4.1). Such a consistency check is shown in Figure 11.

The multipole measurements in Figure 11 indicate that there is no significant detection of the Ly\$\alpha\$ forest-Ly\$\alpha\$ emission cross-correlation. Quantitatively, a line of zero amplitude would lead to \$\chi^2 = 19.8\$ for a total of 21 data points of the monopole, quadrupole, and hexadecapole in the range of $4 \, h^{-1} \, \text{Mpc} < s < 100 \, h^{-1} \, \text{Mpc}$. On the other hand, with the large uncertainties in the data, our model predictions also appear to be consistent with the measurements. The predictions from the best-fit model (solid curves) give a value of \$\chi^2 = 29.5\$ for the above 21 data points, within \$\sim 1.3 \sigma\$ of the expected mean \$\chi^2\$ value. We note that the monopole is consistent with that in Croft et al. (2018), as long as the uncertainties are taken into account (see their Figure 11). Our model has a much lower amplitude than their galaxy-dominated model (Model G), leading to a closer match to the data. This is a manifestation of the lower \$\langle \mu_{\alpha} \rangle\$ value inferred from our quasar-Ly\$\alpha\$ emission cross-correlation measurements.

5. Discussion: Possible Ly α Sources

Our quasar–Ly α emission cross-correlation measurements can be explained by a model with Ly α emission associated with star-forming galaxies (Section 3), and the Ly α forest–Ly α emission cross-correlation measurements are also consistent with such an explanation (Section 4). The model, however, does not provide details on the relation between Ly α emission and galaxies, which we explore in this section.

As shown in Figure 8, the measured Ly\$\alpha\$ luminosity density \$\rho_{\text{Ly}\alpha} = 6.6^{+3.3}_{-3.1} \times 10^{40}\$ erg s\$^{-1}\$ cMpc\$^{-3}\$, computed from our best-fit \$\langle \mu_{\alpha} \rangle\$ under the galaxy-dominated case. This iceberg of Ly\$\alpha\$ emission can hardly be accounted for by Ly\$\alpha\$ emission from LAEs based on observed Ly\$\alpha\$ LFs, as shown in Figure 8 with Ly\$\alpha\$ luminosity densities obtained from integrating the Ly\$\alpha\$ LFs of LAEs down to a low luminosity. For example, the value of \$\rho_{\text{Ly}\alpha}\$ calculated by integrating the LAE LF at \$z = 2.5 \pm 0.1\$ in Sobral et al. (2018) down to 1.75 \times 10^{41}\$ erg s\$^{-1}\$ is $7.4^{+0.8}_{-0.7} \times 10^{39}$ erg s$^{-1}$ cMpc$^{-3}$, only $\sim 12\%$ of our estimate. That is, Lyα emission formally detected from LAEs is only the tip of the iceberg.$

Conversely, if we assume that all the Ly α photons detected in our work are produced by star formation activity and neglect any dust effect on Ly α emission, the implied SFRD ρ_{SFR} approximates the lower bound of the dust-corrected cosmic ρ_{SFRD} determined by UV and IR observations (see Figure 9).

There have to be some other sources responsible for the excessive $Ly\alpha$ emission. In this section, we explore two possible sources based on previous observations and models: $Ly\alpha$ emission within an aperture centered on star-forming galaxies, including LAEs and Lyman-break galaxies (LBGs), with a typical aperture of 2" in diameter in most NB surveys, and $Ly\alpha$ emission outside the aperture usually missed for individual galaxies in NB surveys, commonly called extended or diffuse $Ly\alpha$ halos. We name the two components the inner and outer parts of $Ly\alpha$ emission, respectively. For the outer, diffuse $Ly\alpha$ halo component, we do not intend to discuss its origin here (e.g., Zheng et al. 2011b; Lake et al. 2015) but adopt an observation-motivated empirical model to estimate its contribution.

We argue that almost all star-forming galaxies produce Ly α emission, and actually, significant emission may originate from

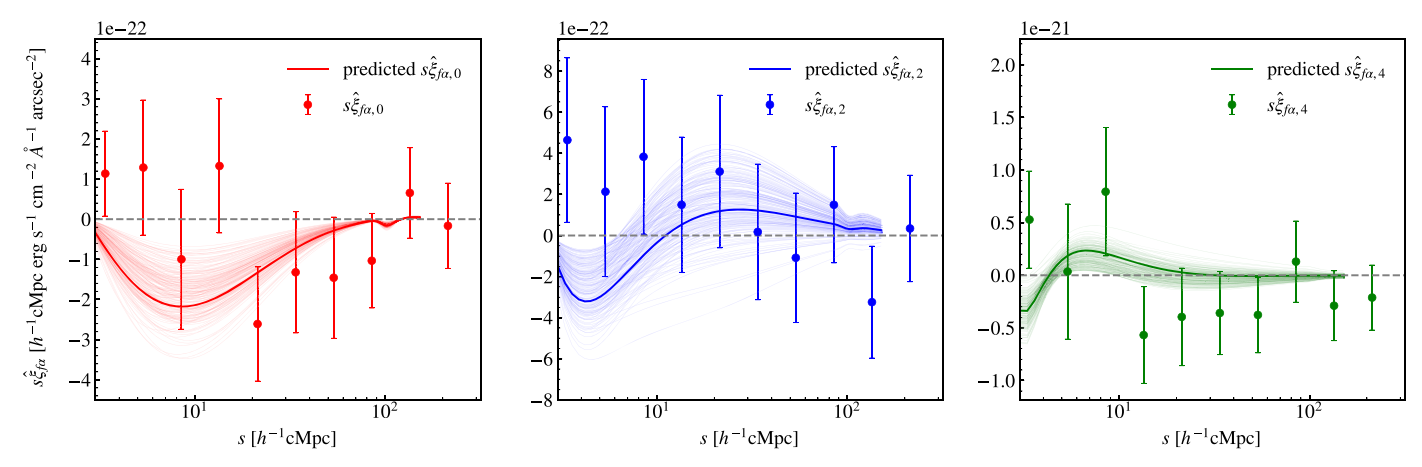


Figure 11. Modified monopole, quadrupole, and hexadecapole of the Ly α forest–Ly α emission cross-correlation as a function of the Ly α forest–Ly α emission pixel pair separation. The data points are the measurements, and the solid curves are the predictions using parameters in literature to describe the Ly α forest and parameters $\langle \mu_{\alpha} \rangle$ and β_{α} derived from fits to the quasar–Ly α emission cross-correlation under the galaxy-dominated scenario. The various solid curves are the predicted modified multipoles from randomly drawing $\langle \mu_{\alpha} \rangle$ and β_{α} from their posterior probability distribution, with the thickest ones from adopting the best-fit parameters.

their halos. This should contribute to the bulk of faint diffuse $Ly\alpha$ emission in the universe, as detected in this work.

5.1. Inner Part of Ly\alpha Emission for UV-selected Star-forming Galaxies

A large portion of LBGs exhibit Ly α emission, though their rest-frame equivalent width (REW) might not satisfy the criteria for LAE selections (Shapley et al. 2003; de La Vieuville et al. 2020) if measured with the typical aperture of 2" in diameter in NB surveys. Ly α emission has also been detected in deep stacks of luminous and massive LBGs (Steidel et al. 2011) and in individual UV-selected galaxies in recent MUSE Extremely Deep Field (MXDF) observations (Kusakabe et al. 2022).

Dijkstra & Wyithe (2012) reported the Ly α REW distribution of \sim 800 $z\sim$ 3 LBGs spectroscopically observed by Shapley et al. (2003) with 1.4 slits, which can be described well by an exponential function. This sample includes both Ly α emission (REW > 0 Å) and Ly α absorption (REW < 0 Å) within the central aperture. Combined with this empirical model of Ly α REW distribution for star-forming galaxies, we perform integration over the UV LF to obtain the corresponding Ly α luminosity density:

$$\rho_{\mathrm{Ly}\alpha}^{\mathrm{inner}} = \int_{M_{\mathrm{UV,min}}}^{M_{\mathrm{UV,max}}} \left[\langle L_{\alpha}(M_{\mathrm{UV}}) \rangle \Phi_{\mathrm{UV}}^{e}(M_{\mathrm{UV}}) + \langle L_{\alpha}^{\mathrm{Abs}}(M_{\mathrm{UV}}) \rangle \Phi_{\mathrm{UV}}^{a}(M_{\mathrm{UV}}) \right] dM_{\mathrm{UV}}$$
(25)

where $\langle L_{\alpha}(M_{\rm\,UV}) \rangle$ is the mean Ly α luminosity within the aperture of the REW > 0 Å population at a given UV luminosity and $\langle L_{\alpha}^{\rm Abs}(M_{\rm UV}) \rangle$ is the absorption of the REW < 0 Å population making a negative contribution. The function $\Phi^e_{\rm\,UV}$ is the UV LF for the REW > 0 Å population, which is the overall UV LF $\Phi_{\rm\,UV}$ multiplied by the UV luminosity dependent fraction of such a population, and $\Phi^a_{\rm\,UV}$ is the UV LF for the REW < 0 Å population. More details on the calculations in our adopted model are presented in Appendix B.

We select five observed UV LFs around $z\approx 2.4$ from the literature (Table 1), and calculate the corresponding Ly α luminosity densities, which are shown in Table 2.

We note that the distribution of $Ly\alpha$ REW within the central aperture is mainly determined by three factors: the intrinsic REW from photoionization and recombination in the H II region of star-forming galaxies, the dust extinction, and the scattering-induced escape fraction. The empirically modeled $Ly\alpha$ REW distribution in Dijkstra & Wyithe (2012) we adopt reflects the combination of the three factors.

5.2. Outer Part of Ly\alpha Emission from Galaxy Halos

As discussed before, many previous works have reported detections of extended Ly α emission around high-redshift galaxies, either by discoveries of Ly α halos/blobs around bright individual star-forming galaxies through ultradeep exposures (Steidel et al. 2000; Matsuda et al. 2004, 2011; Wisotzki et al. 2016; Leclercq et al. 2017; Kusakabe et al. 2022), or by employing stacking analyses on large samples (Steidel et al. 2011; Matsuda et al. 2012; Momose et al. 2014, 2016; Xue et al. 2017). Most extended Ly α -emitting halos are discovered around LAEs (Wisotzki et al. 2016; Leclercq et al. 2017); they are also prevalent around non-LAEs, e.g., UV-selected galaxies, due to a significant amount of cool/warm gas in their CGM (Steidel et al. 2011; Kusakabe et al. 2022).

The cumulative fraction of the large-aperture Ly α flux, shown in Figure 10 of Steidel et al. (2011), indicates that the 2" aperture adopted by typical deep NB/mediumband LAE surveys could miss ~50% of the Ly α emission for LBGs with net (positive) Ly α emission. Thus Equation (25) could underestimate the total Ly α flux from REW > 0 Å galaxies roughly by a factor of 2. For galaxies whose inner parts present net Ly α absorption, the existence of extended Ly α halos has been strongly confirmed by the sample with Ly α REW < 0 Å in Steidel et al. (2011), whose radial SB profile outside 10 kpc is qualitatively similar to that of the non-LAE subsamples.

Given the above observational results, we adopt the reasonable model that all star-forming galaxies, whether showing Ly α emission or absorption within the central aperture, have Ly α -emitting halos. Based on the strong anticorrelation between the Ly α luminosities of Ly α halos and the corresponding UV magnitudes reported in Leclercq et al. (2017), we assume that the Ly α luminosity from halos of

Table 1
A Compilation of the Derived Schechter Function Parameters for the Galaxy UV LFs Adopted in This Work

Source	z	$\lambda_{\mathrm{UV}}^{\mathrm{a}}(\mathring{\mathrm{A}})$	$M^{^*}$	$\Phi^* (10^{-3} \text{cMpc}^{-3})$	α
Reddy & Steidel (2009)	2.3	1700	-20.70 ± 0.11	2.75 ± 0.54	-1.73 ± 0.07
Sawicki (2012)	2.2	1700	-21.00 ± 0.50	2.74 ± 0.24	-1.47 ± 0.24
Parsa et al. (2016)	2.25	1700	-19.99 ± 0.08	6.20 ± 0.77	-1.31 ± 0.04
Bouwens et al. (2015)		1600	-20.89 + 0.12z	$0.48 \times 10^{-0.19(z - 6)}$	-1.85 - 0.09(z - 6)
Extrapolation ^b	2.4		-20.60	2.3	-1.53
Parsa et al. (2016)	•••	1700	$\frac{-35.4(1+z)^{0.524}}{1+(1+z)^{0.678}}$	-0.36z + 2.8	-0.106z - 1.187
Extrapolation ^c	2.4		-20.41	1.9	-1.44

Notes.

Source	Z.	$\rho_{\rm Ly\alpha} \ (10^{40} {\rm erg s^{-1} cMpc^{-3}})$			
	~	Inner ^a	Outer ^b	Total ^e	
Reddy & Steidel (2009)	2.3	3.82	4.17	8.00	
Sawicki (2012)	2.2	2.10	2.71	4.81	
Parsa et al. (2016)	2.25	1.83	2.05	3.88	
Bouwens et al. (2015)	2.4	1.61	1.87	3.49	
Extrapolation ^d					
Parsa et al. (2016)	2.4	0.97	1.12	2.09	
Extrapolation ^d					

Notes. See Sections 5.1 and 5.2 for more details.

galaxies with REW < 0 Å depends on $M_{\rm UV}$ only. We further assume that it is equal to the inner part originating from the REW > 0 Å galaxy population at a given $M_{\rm UV}$ (Steidel et al. 2011). Therefore we express the total contribution to the Ly α luminosity density from the outer part as

$$\rho_{\mathrm{Ly}\alpha}^{\mathrm{outer}} = \int_{M_{\mathrm{UV,min}}}^{M_{\mathrm{UV,max}}} \langle L_{\alpha}(M_{\mathrm{UV}}) \rangle \Phi_{\mathrm{UV}}(M_{\mathrm{UV}}) dM_{\mathrm{UV}}, \qquad (26)$$

where Φ_{UV} denotes the UV LF for the entire population (see Appendix B).

Clearly, the total Ly α luminosity density should be $\rho_{\text{Ly}\alpha}^{\text{tot}} = \rho_{\text{Ly}\alpha}^{\text{inner}} + \rho_{\text{Ly}\alpha}^{\text{outer}}$. Note that the total Ly α luminosity density estimated from the model is just a lower limit as discussed in Appendix B, since we (1) adopt a constant scaling

factor for the Dijkstra & Wyithe (2012) empirical model and (2) use this empirical model that is designed for the REW > 0 Å population to describe the REW < 0 Å one. A brief summary of the estimated Ly α luminosity densities is made in Table 2 and Figure 12. As revealed by Figure 12, the total Ly α luminosity density derived from our model is consistent with our detection within 1σ (or $\sim 1.3\sigma$ when using the z=2.4 UV LF in Parsa et al. 2016). We argue that star-forming galaxies, which contain an inner part of Ly α emission that can be captured by aperture photometry in deep NB surveys and an outer part of Ly α emission that can be captured from their halos, usually outside the aperture, could produce sufficient Ly α emission to explain our detection from the quasar–Ly α emission cross-correlation measurement.

Our derived $\rho_{\mathrm{Ly}\alpha}$ is higher than the result of Wisotzki et al. (2018), who used MUSE observations of extended $\mathrm{Ly}\alpha$ emission from LAEs to infer a nearly 100% sky coverage of $\mathrm{Ly}\alpha$ emission. The LAE sample they used were selected from the Hubble Deep Field South and the Hubble Ultra Deep Field, a subset of LAEs whose $\mathrm{Ly}\alpha$ LFs have been analyzed in Drake et al. (2017a) and Drake et al. (2017b) (though the sample in Wisotzki et al. 2018 contains a few additional LAEs). As shown in Figure 8, the $\rho_{\mathrm{Ly}\alpha}$ estimated in Drake et al. (2017a) is lower than ours, too. Our result implies that Wisotzki et al. (2018) may have underestimated the $\mathrm{Ly}\alpha$ sky coverage at a given SB level when simply focusing on LAEs and ignoring the diffuse $\mathrm{Ly}\alpha$ emission from faint UV-selected galaxies.

As shown in Figure 12, about half of the detected Ly α photons come from the inner part of galaxies. By assuming that they all stem from star formation activity, we estimate the escape fraction $f_{\rm esc}$ for these Ly α photons to be roughly $0.21^{+0.21}_{-0.11}$, where the cosmic intrinsic Ly α luminosity density due to star formation is calculated based on the cosmic SFRD shown in Figure 9, yielding $1.44^{+10.1}_{-6.1} \times 10^{41}\,\mathrm{erg}\,\mathrm{s}^{-1}\,\mathrm{Mpc}^{-3}$. While the estimated $f_{\rm esc}$ appears consistent with previous work within 1σ uncertainties (e.g., $\sim 10\%$ in Chiang et al. 2019), we emphasize that the galaxy population involved in our modeling is different from the LAEs in typical NB surveys. We include galaxies with small Ly α REWs usually not identified as LAEs, which boost our estimate for $f_{\rm esc}$ as compared with LAE-derived ones.

^a Rest-frame UV wavelength where the UV LF is measured. Note that λ_{UV} for Bouwens et al. (2015) is 1600 Å, while the empirical model in Dijkstra & Wyithe (2012) as summarized in Appendix B.1 adopts 1700 Å. We just assume that UV LFs are not sensitive to such a subtle difference in λ_{UV} .

Extrapolation of the Schechter parameters of the UV LF to z = 2.4 adopting the best-fitting formula in Bouwens et al. (2015) for the redshift evolution.

^c Extrapolation to z = 2.4, based on the simple parametric fits to published Schechter parameters in Parsa et al. (2016). Note that this fitting is meant to illustrate the overall evolutionary trend, and not to indicate a best estimate of true parameter evolution.

^a Lyα luminosity density from emission that would be captured within an aperture 2" in diameter, computed from Equation (25). Galaxies with Lyα REW > 0 Å contribute a positive part and the Lyα REW < 0 Å population contribute a negative one.

^b Ly α luminosity density from emission outside the 2" aperture for all galaxies, i.e., the diffuse Ly α halo component, computed from Equation (26). At a given UV luminosity, we assume that the populations with central REW > 0 Å and REW < 0 Å have the same diffuse halo Ly α luminosity, which is set to be the same as that from the inner part of the REW > 0 Å population in our model based on the results in Steidel et al. (2011).

^c Total Ly α luminosity density contributed by the two components discussed above.

d Same as in Table 1.

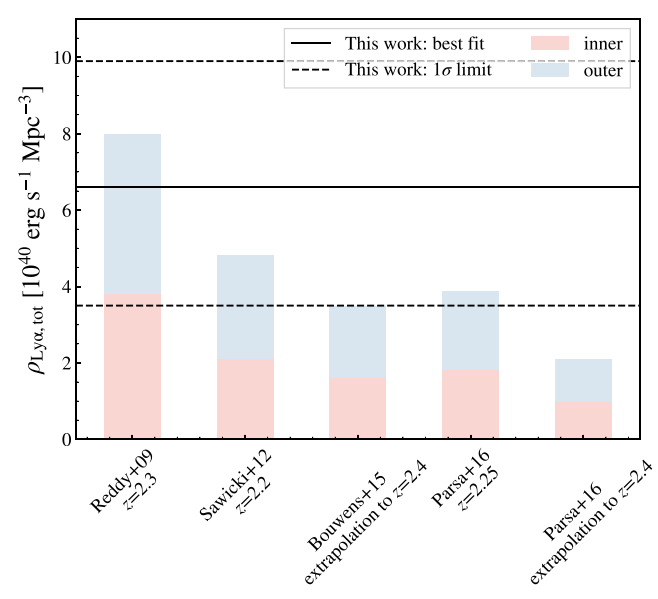


Figure 12. Ly α luminosity density computed in our model by integrating different observed UV LFs. Different colors denote the inner and outer Ly α parts, as described in Table 2 in detail. The model Ly α luminosity densities are compared with that inferred from our quasar–Ly α emission cross-correlation measurements, 6.6×10^{40} erg s⁻¹ cMpc⁻³ (solid) with 1σ error bars (dashed) of $\pm 3.2 \times 10^{40}$ erg s⁻¹ cMpc⁻³.

6. Summary and Conclusion

In this work, we have performed a cross-correlation analysis of the SDSS BOSS/eBOSS LRG residual spectra at wavelengths $\lambda=3647$ – $5471\,\mathring{\rm A}$ and DR16 quasars at a redshift range of 2 < z < 3.5. This enables measurements of the cross-correlation between quasar position and Ly α emission intensity (embedded in the residual LRG spectra) at a median redshift $z \sim 2.4$. The Ly α SB profile around quasars is obtained by projecting our cross-correlation results into a pseudo-NB, and truncated forms of the monopole, quadrupole, and hexadecapole of the quasar–Ly α emission cross-correlation are computed by discarding small-scale signals within $r_{\perp} < 4 \ h^{-1}$ cMpc.

Our work improves on that in Croft et al. (2018) by making use of the final SDSS-IV release of LRG spectra and a quasar catalog. While our $Ly\alpha$ SB profile measurements are consistent with those in Croft et al. (2018), our inferred large-scale clustering amplitude is about 2.2 times lower. Although the absolute uncertainty in our work is about 25% lower, the lower clustering amplitude leads to a larger fractional uncertainty. This is a reflection of our more rigorous treatment of possibly contaminated fibers and our exclusion of small-scale signals in modeling the multipoles. With this lower amplitude, our measured $Ly\alpha$ forest– $Ly\alpha$ emission cross-correlation can also be consistently explained.

Like that in Croft et al. (2018), on sub-Mpc scales the obtained $Ly\alpha$ SB forms a natural extrapolation of that observed from luminous $Ly\alpha$ blobs on smaller scales (Borisova et al. 2016; Cai et al. 2019). Unlike Croft et al. (2018), we find that the amplitudes of the large-scale $Ly\alpha$ SB and quasar- $Ly\alpha$ emission cross-correlation cannot result from the $Ly\alpha$ emission around quasars, as this would require the average $Ly\alpha$ luminosity of quasars to be about two orders of magnitude higher than observed given their rather low number density.

To figure out the most likely sources that contribute to the detected Ly α signals, we construct a simple analytical

model that combines the SB profile and multipole measurements. The inferred Ly α luminosity density, $6.6^{+3.3}_{-3.1} \times$ 10⁴⁰ erg s⁻¹ cMpc⁻³, is much higher than those from integrating the Ly α LFs of LAEs. We fix the luminosity-weighted bias of galaxies b_{α} to 3 in our modeling, which turns out to be a good estimate. But bear in mind that the luminosity density scales with $3/b_{\alpha}$ if b_{α} deviates from that value. Our model rules out the possibility that the diffuse emission is due to reprocessed energy from the quasars themselves, and supports the hypothesis that star-forming galaxies clustered around are responsible for the detected signal. For the Ly α forest–Ly α emission cross-correlation, the prediction from our model matches the measurement, although the current measurement is consistent with a null detection given the low signal-to-noise ratio. We argue that most star-forming galaxies exhibit Ly α emission. These include galaxy populations with either Ly α emission or Ly α absorption at the center, and both populations have diffuse Ly α -emitting halos, which are usually missed in individual LAEs from deep NB surveys. Our estimates based on the empirical model of Dijkstra & Wyithe (2012) and the observed UV LFs of star-forming galaxies are able to match the Ly α luminosity density inferred from our cross-correlation measurements. The picture is supported by stacked analysis from NB surveys (e.g., Steidel et al. 2011) and by integral field unit observations of Ly α emission associated with UV-selected galaxies (e.g., Kusakabe et al. 2022).

Our work shows the enormous promise of Ly α IM as a probe of large-scale structures. One can also utilize this technique to explore the intensity of other spectral lines, once a larger data set is provided. A next-generation cosmological spectroscopic survey, the ongoing survey of the Dark Energy Spectroscopic Instrument (DESI; DESI Collaboration et al. 2016), will enlarge the galaxy/quasar survey volume at least by an order of magnitude compared to SDSS BOSS/eBOSS. We expect the IM technique carried out in DESI will bring us new insights into the universe. Deep surveys of Ly α emission around star-forming galaxies, especially the UV-selected population (e.g., Kusakabe et al. 2022), will shed light on IM measurements and provide inputs for building the corresponding model. Moreover, more realistic modeling of physical processes such as radiative transfer and the quasar proximity effect should be considered to advance our understanding of the Ly α emission iceberg in the universe.

We thank Kyle Dawson, Rupert Croft, and Coast Zhang for useful discussions. X.L. and Z.C. are supported by the National Key R&D Program of China (grant No. 2018YFA0404503) and the National Science Foundation of China (grant No. 12073014). Z.Z. is supported by NSF grant AST-2007499.

Funding for SDSS-IV has been provided by the Alfred P. Sloan Foundation, the U.S. Department of Energy Office of Science, and the Participating Institutions.

SDSS-IV acknowledges support and resources from the Center for High Performance Computing at the University of Utah. The SDSS website is www.sdss.org. SDSS-IV is managed by the Astrophysical Research Consortium for the participating institutions of the SDSS Collaboration including the Brazilian Participation Group, the Carnegie Institution for Science, Carnegie Mellon University, the Center for Astrophysics | Harvard & Smithsonian, the Chilean Participation Group, the French Participation Group, Instituto de Astrofísica de Canarias, the Johns Hopkins University, the

Kavli Institute for the Physics and Mathematics of the Universe (IPMU)/the University of Tokyo, the Korean Participation Group, Lawrence Berkeley National Laboratory, Leibniz Institut für Astrophysik Potsdam (AIP), Max-Planck-Institut für Astronomie (MPIA Heidelberg), Max-Planck-Institut für Astrophysik (MPA Garching), Max-Planck-Institut für Extraterrestrische Physik (MPE), the National Astronomical Observatories of China, New Mexico State University, New York University, the University of Notre Dame, Observatário Nacional/MCTI, the Ohio State University, Pennsylvania State University, Shanghai Astronomical Observatory, the United Kingdom Participation Group, Universidad Nacional Autónoma de México, the University of Arizona, the University of Colorado Boulder, the University of Oxford, the University of Portsmouth, the University of Utah, the University of Virginia, the University of Washington, the University of Wisconsin, Vanderbilt University, and Yale University.

Appendix A Correcting Measurement Systematics

Dealing with possible contamination is a difficult problem in all IM experiments. Since the expected signals in our measurement have gone beyond the detection capability of any current instruments, it is crucial to remove possible systematics. In this section we discuss three main sources of potential contamination—cross-talk effect among spectra in adjacent fibers, correlation at $r_{\parallel}=0$ for pixel–pixel pairs, and spurious signals on larger scales—and then demonstrate that we have removed them carefully from our measurement.

A.1. Quasar Stray Light Contamination

The BOSS/eBOSS spectrograph has 1000 fibers per plate, which disperse light onto the same 4096-column CCD. Light from one fiber would possibly leak into the extraction aperture for another fiber, but the level of this light contamination is negligible in the SDSS data reduction pipeline. However, our IM technique reaches far beyond the instrument capability ($\sim 10^{-17} \, \mathrm{erg \ s^{-1} \ cm^{-2} \ \AA^{-1} \ arcsec^{-2}}$), so this light contamination should be treated cautiously. When cross-correlating quasar–LRG spectrum pixels, the cross-correlation between quasars and their leakage into LRG spectra will lead to a contamination 3–4 orders of magnitude higher than the targeted Ly α signals, due to the bright and broad Ly α features of quasars.

In Croft et al. (2016), quasar stray light contamination was removed through discarding any quasar-LRG spectrum pixel pairs once on the CCD the quasar was within five fibers away from the LRG, i.e., $\Delta_{\rm fiber}$ < 5. Moreover, Croft et al. (2018) reported that the remaining quasar stray light would still lead to contamination as a result of the quasar clustering effect: an LRG fiber with $\Delta_{\text{fiber}} \geqslant 5$ from a quasar fiber may be contaminated by another quasar, and if this contamination is not corrected for, the cross-correlation between Ly α emission in the LRG fiber and the first quasar would have the quasar clustering signal imprinted. They found that the quasar clustering effect would reach 50% of the signal in Croft et al. (2016) on scales of $|r_{\perp}| < 10 \,h^{-1}\,\mathrm{Mpc}$ and $|r_{\parallel}| < 10 \, h^{-1} \,\mathrm{Mpc}$. Croft et al. (2018) corrected such an effect by generating a set of mock spectra that contained quasar contaminating light only and performing the same

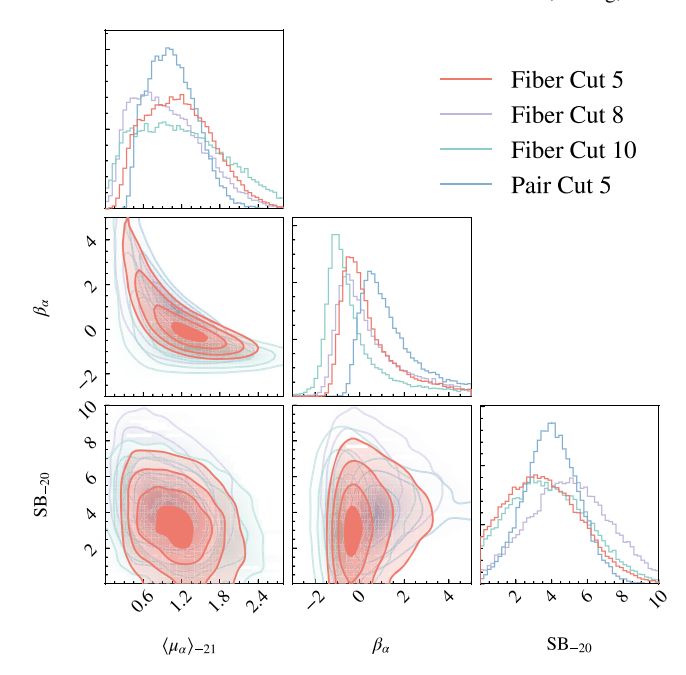


Figure 13. A test for the robustness of our fiducial sample selection, by performing joint fits to the multipoles and SB profiles of quasar–Ly α emission cross-correlation after different sample selections. The model parameters are the same as those in Figure 7. Fiber Cut 5 refers to the sample where any LRG fiber with $\Delta_{\rm fiber} < 5$ from a quasar fiber is excluded, which is the fiducial sample for our measurements; Fiber Cut 8 and Fiber Cut 10 refer to $\Delta_{\rm fiber} < 8$ and $\Delta_{\rm fiber} < 10$, respectively. Pair Cut 5 refers to the sample in which a quasar–LRG spectrum pixel pair is excluded if it satisfies $\Delta_{\rm fiber} < 5$, i.e., the method adopted in Croft et al. (2018).

cross-correlation procedure to measure the intensity of clustering. Then the clustering signal from the mock was subtracted from their originally measured signals.

The key of the algorithm in Croft et al. (2018) is to estimate the light leakage fraction so that cross-correlation of mock spectra can precisely reproduce the quasar clustering effect. The fraction measured in Croft et al. (2016) is no longer applicable to our sample spectra, however, due to the recent updates on the DR16 optical spectrum pipeline.⁵ In our measurement, to be conservative, instead we exclude any LRG fiber once it is within five fibers or fewer away from a quasar fiber, and this fiducial sample selection will remove both quasar stray light contamination and the quasar clustering effect simultaneously. We also repeat the algorithm introduced in Croft et al. (2018), removing quasar clustering systematics by subtracting the cross-correlation pattern produced by mock spectra, and then measure the corresponding multipoles and SB profiles. To ensure the robustness of our fiducial sample selection, i.e., the exclusion of all LRG fibers of $\Delta_{\text{fiber}} < 5$, we perform the same fitting procedure mentioned in Section 3.4 under the galaxy-dominated assumption for test cases with various sample selections. A comparison of results with differently selected samples is demonstrated in Figure 13. The result of $\Delta_{\rm fiber}$ < 5 LRG exclusion is in fact consistent with that of $\Delta_{\rm fiber}\!<\!8$ and $\Delta_{\rm fiber}\!<\!10$ within $1\sigma,$ implying that fourfiber fiducial selection can remove the contamination well. It in general accords with the result of $\Delta_{\rm fiber}$ < 5 pair exclusion, i.e., the method used in Croft et al. (2018), though there is a tiny

⁵ https://www.sdss.org/dr16/spectro/pipeline/

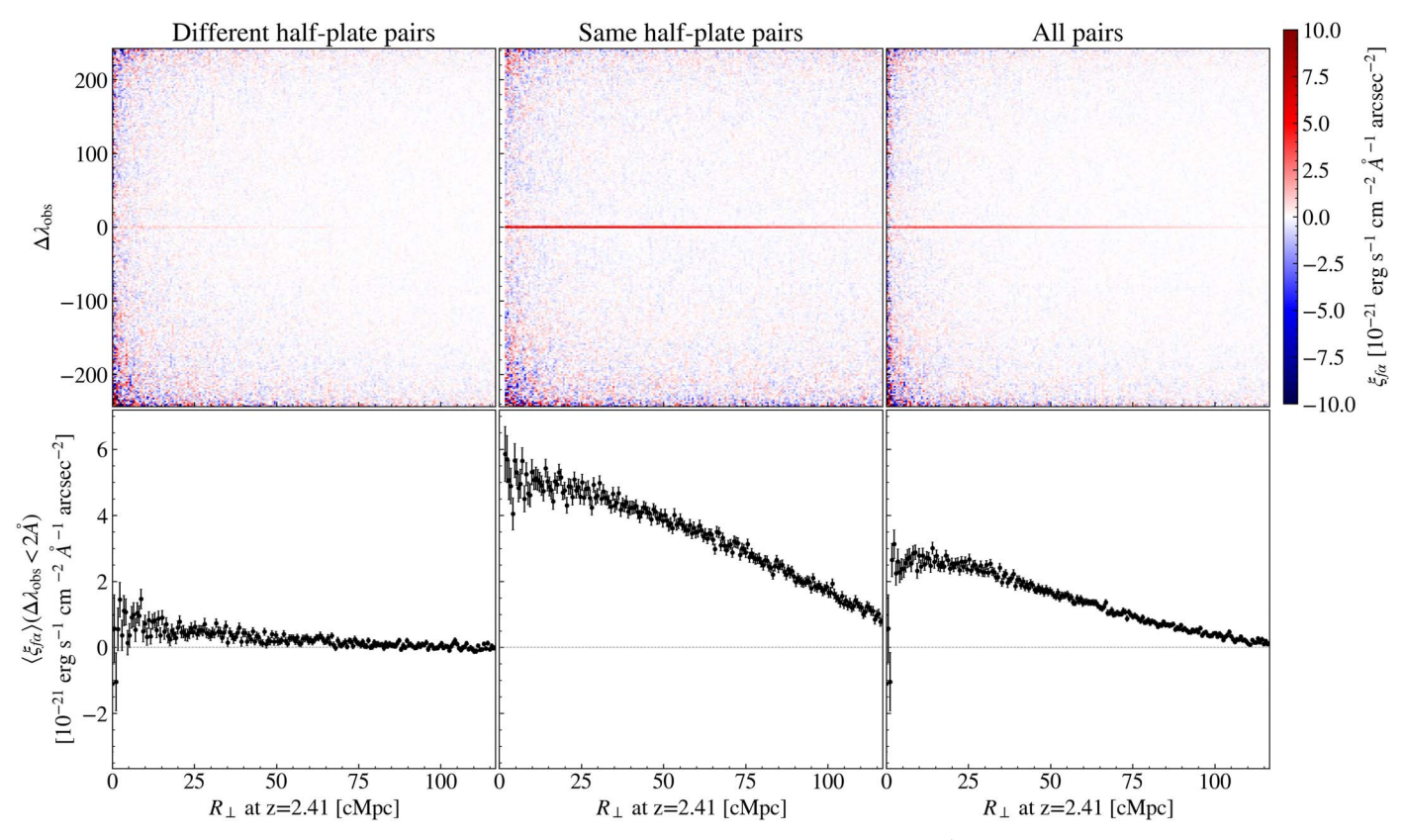


Figure 14. Ly α forest—Ly α emission pixel—pixel correlation as a function of observed wavelength separations $\Delta\lambda_{obs}$ and transverse separations at a redshift of 2.41. Different—half—plate pairs refers to the sample in which the selected pixel pairs reside on different half-plates; Same—half—plate pairs refers to the sample in which all pairs are on the same half-plates. All pairs refers to the sample without preference for the plates/fibers. The bottom panels show the correlations averaged within 2 Å at $\Delta\lambda_{obs} \sim 0$.

offset in best-fit β_{α} and the uncertainties of the three parameters from the latter are smaller.

A.2. $r_{\parallel} = 0$ Correlation for Pixel-Pixel Pairs

In measuring the Ly α forest–Ly α emission cross-correlation, we need to remove an artifact of correlation around $r_{\parallel}=0$, introduced by the spectral pipeline.

In BOSS/eBOSS, each half-plate has ~500 fibers (450 science fibers and ~40 sky fibers) with two spectrographs. Sky subtraction for individual spectra is done independently for each spectrograph. Poisson fluctuations in sky spectra will induce correlations in those spectra obtained with the same spectrograph at the same observed wavelength (Bautista et al. 2017; du Mas des Bourboux et al. 2019, 2020). That is, a positive correlation is expected for spectrum pixel pairs on the same half-plates at $\Delta\lambda_{\rm obs} = 0$, leading to an excess correlation in $r_{\parallel} = 0$ bins. Furthermore, the continuum fitting procedure designed for Ly α forest transmission fields may smooth the excess correlation at $r_{\parallel} = 0$, extending it to larger $|r_{\parallel}|$. Therefore we reject Ly α forest-Ly α emission pixel pairs once they are observed on the same half-plate.

To evaluate how this same-spectrograph-induced systematics would contaminate the signals and whether we have fully removed it, we perform measurements of the cross-correlation between Ly α forest transmission pixels and Ly α emission pixels, as a function of their observed wavelength separations

 $\Delta \lambda_{\rm obs}$ and transverse separations $\Delta \theta$,

$$\xi_{f\alpha}(\Delta\lambda_{\text{obs}}, \Delta\theta) = \frac{1}{\sum_{i=1}^{N} w_{ri,\alpha} w_{ri,f}} \times \sum_{i=1}^{N} w_{ri,\alpha} w_{ri,f} \Delta_{\mu,ri}(\lambda_{\text{obs}}, \theta) \delta_{f,ri} \times (\lambda_{\text{obs}} + \Delta\lambda_{\text{obs}}, \theta + \Delta\theta), \tag{A1}$$

where $\Delta\theta$ can be easily converted to the transverse comoving separation at z = 2.41 by $R_{\perp} = \Delta \theta \cdot D_C(z = 2.41)$. The crosscorrelation results of different-half-plate pixel pairs, same-halfplate pixel pairs, and all pixel pairs without selection preference are shown in Figure 14. The contamination at $\lambda_{obs} = 0$ for samehalf-plate pairs reaches several $10^{-21} \, \mathrm{erg \ s^{-1} \ cm^{-2} \ \AA^{-1} \ arcsec^{-2}}$ (middle panel), even stronger than the targeted signals, stressing the necessity of rejecting same-half-plate pixel pairs. While the contamination is largely removed when we only use differenthalf-plate pixel pairs (left panel), there still appears to be a residual weak correlation at $\Delta \lambda_{\rm obs} \sim 0$, not expected from pure sky subtraction effects. The exact source of such a weak correlation at $\Delta \lambda_{\rm obs} \sim 0$ may be related to some details in the processing procedure in the spectral pipeline. To proceed, we adopt a conservative method to remove the effect of this weak correlation by discarding any signal within $|r_{\parallel}| < 4$ cMpc, at the expense of the signal-to-noise ratio of our measurement, i.e., slightly reducing it.

A.3. Large-scale Correction

As discussed in Croft et al. (2016), one may find nonzero cross-correlation for large pair separation with no physical significance that we are concerned about. We correct this spurious signal by subtracting the average correlation over $80\text{--}400\ h^{-1}$ Mpc along both the line-of-sight and orthogonal directions, following the method described in Croft et al. (2016).

Appendix B Model for Ly α Luminosity Density Contributed by Star-forming Galaxies

In our model, star-forming galaxies dominate the $Ly\alpha$ luminosity density. We first review the Dijkstra & Wyithe (2012) model for the REW distribution of $Ly\alpha$ emission from an inner aperture around star-forming galaxies. With such an REW distribution, we present our model of $Ly\alpha$ luminosity density from contributions of $Ly\alpha$ emission within the inner aperture and from the outer halo.

B.1. Model for Lya REW Distribution of UV-selected Galaxies

Dijkstra & Wyithe (2012) modeled the conditional probability density function (PDF) for the REW of Ly α emission (from the central aperture around LBGs) using an exponential function whose scaling factor REW $_c$ depends on $M_{\rm UV}$ and z,

$$P(\text{REW}|M_{\text{UV}}) = \begin{cases} \mathcal{N} \exp\left(-\frac{\text{REW}}{\text{REW}_c}\right), & \text{REW} \in (x_{\text{min}}, x_{\text{max}})\\ 0, & \text{otherwise} \end{cases}$$
(B1)

where \mathcal{N} denotes the normalization constant. The choice of normalization factor \mathcal{N} allows the assumption that all dropout galaxies have $x_{\min} \leqslant \text{REW} \leqslant x_{\max}$:

$$\mathcal{N}^{-1} = \text{REW}_c \left[\exp \left(-\frac{x_{\text{min}}}{\text{REW}_c(M_{\text{UV}})} \right) - \exp \left(-\frac{x_{\text{max}}}{\text{REW}_c(M_{\text{UV}})} \right) \right].$$
 (B2)

To match the $M_{\rm UV}$ dependence of the observed fraction of LAEs (REW > 50 Å) in dropout galaxies, they fixed $x_{\rm max} = 300$ and assumed $x_{\rm min} \equiv -a_1$ (both in units of Å):

$$a_{1} = \begin{cases} 20 & M_{\text{UV}} < -21.5\\ 20 - 6(M_{\text{UV}} + 21.5)^{2} & -21.5 \leqslant M_{\text{UV}} < -19. \end{cases}$$
 (B3)

In their fiducial model, REW_c evolves with $M_{\rm UV}$ and z:

$$REW_c(M_{UV}, z) = REW_{c,0} + \mu_1(M_{UV} + 21.9) + \mu_2(z - 4),$$
(B4)

where the best-fitting parameters are REW_{c,0} = 23 Å, μ_1 = 7 Å, and μ_2 = 6 Å. Note that the fitting formula applies only in the observed range of UV magnitudes and the evolution is frozen for $M_{\rm UV} > -19$. However, in our analysis we adopt a constant REW_c = 22 Å, which depicts the REW distribution of the 400 brightest LBG sample of Shapley et al. (2003) well but underpredicts the faint-end LAE fraction, as discussed in Appendix A1 of Dijkstra & Wyithe (2012). With this constant REW_c, we would underestimate the Ly α luminosity

contributed by UV-faint galaxies, and the total estimated Ly α emission would be a lower limit.

The ${\rm Ly}\alpha$ luminosity at a given REW and UV luminosity can be expressed as

$$L_{\alpha}(\text{REW}, M_{\text{UV}}) = L_{\text{UV},\nu}(\nu_{\alpha}/\lambda_{\alpha})(\lambda_{\text{UV}}/\lambda_{\alpha})^{-\beta-2} \cdot \text{REW}, \quad (B5)$$

with the absolute AB magnitude $M_{\rm UV}=-2.5\log[L_{\rm UV,\nu}/({\rm erg~s^{-1}Hz^{-1}})]+51.6$. The parameter β characterizes the slope of the UV continuum, such that $L_{\rm UV,\lambda}=\nu L_{\rm UV,\nu}/\lambda\propto\lambda^{\beta}$. We adopt $\lambda_{\rm UV}=1700\,{\rm \mathring{A}}$ and fix $\beta=-1.7$ as in Dijkstra & Wyithe (2012). The adopted wavelength is the same as that in the UV LF measurements (Table 1), except for the Bouwens et al. (2015) UV LF (measured at 1600 Å). In our calculation, we ignore the slight wavelength shift in the Bouwens et al. (2015) UV LF, as the effect in the UV luminosity computation is less than 2%.

B.2. Model for the Inner and Outer Ly\alpha Emission Components

We separate star-forming galaxies into two populations based on the case of Ly α radiation within the central 2'' aperture, one with Ly α emission (REW > 0) and one with Ly α absorption (REW < 0). We can express the corresponding UV LFs as

$$\Phi_{\text{UV}}^{e}(M_{\text{UV}}) = \frac{\int_{0}^{+\infty} P(\text{REW}|M_{\text{UV}})d\text{REW}}{\int_{-\infty}^{+\infty} P(\text{REW}|M_{\text{UV}})d\text{REW}}$$

$$\times \Phi_{\text{UV}}(M_{\text{UV}}) \tag{B6}$$

for the REW > 0 population and

$$\Phi_{\text{UV}}^{a}(M_{\text{UV}}) = \frac{\int_{-\infty}^{0} P(\text{REW}|M_{\text{UV}})d\text{REW}}{\int_{-\infty}^{+\infty} P(\text{REW}|M_{\text{UV}})d\text{REW}}$$

$$\times \Phi_{\text{UV}}(M_{\text{UV}}) \tag{B7}$$

for the REW < 0 population, where $P(\text{REW}|M_{\text{UV}})$ is the REW distribution for galaxies with UV luminosity M_{UV} . Clearly, by construction, $\Phi^e_{\text{UV}} + \Phi^a_{\text{UV}} = \Phi_{\text{UV}}$. Note that we formally use $-\infty$ and $+\infty$ for clarity, while the true cutoff thresholds are encoded in $P(\text{REW}|M_{\text{UV}})$, which takes the form of Equation (B1) if we adopt the Dijkstra & Wyithe (2012) model.

The mean Ly α luminosity within the 2" aperture of the REW > 0 population at a given UV luminosity is

$$\langle L_{\alpha}(M_{\text{UV}})\rangle = \frac{\int_{0}^{+\infty} L_{\alpha}(\text{REW}, M_{\text{UV}})P(\text{REW}|M_{\text{UV}})d\text{REW}}{\int_{0}^{+\infty} P(\text{REW}|M_{\text{UV}})d\text{REW}}.$$
 (B8)

where $L_{\alpha}(\text{REW}, M_{\text{UV}})$ can be calculated through Equation (B5). Figure 15 presents the evolution of $\langle L_{\alpha}(M_{\text{UV}}) \rangle$, Φ^a_{UV} , and Φ^e_{UV} with M_{UV} in our model. We also show the expected Ly α luminosity for the star formation rate (SFR) associated with the UV luminosity, calculated through the following relations: an SFR of 1 M_{\odot} yr⁻¹ corresponds to UV luminosity $L_{\nu} = 1.4 \times 10^{-28}\,\mathrm{erg}\,\mathrm{s}^{-1}$ Hz⁻¹ and Ly α luminosity $L_{\alpha} = 1.1 \times 10^{42}\,\mathrm{erg}\,\mathrm{s}^{-1}$. It is much higher than our modeled Ly α luminosity, consistent with the measurements in Figure 9.

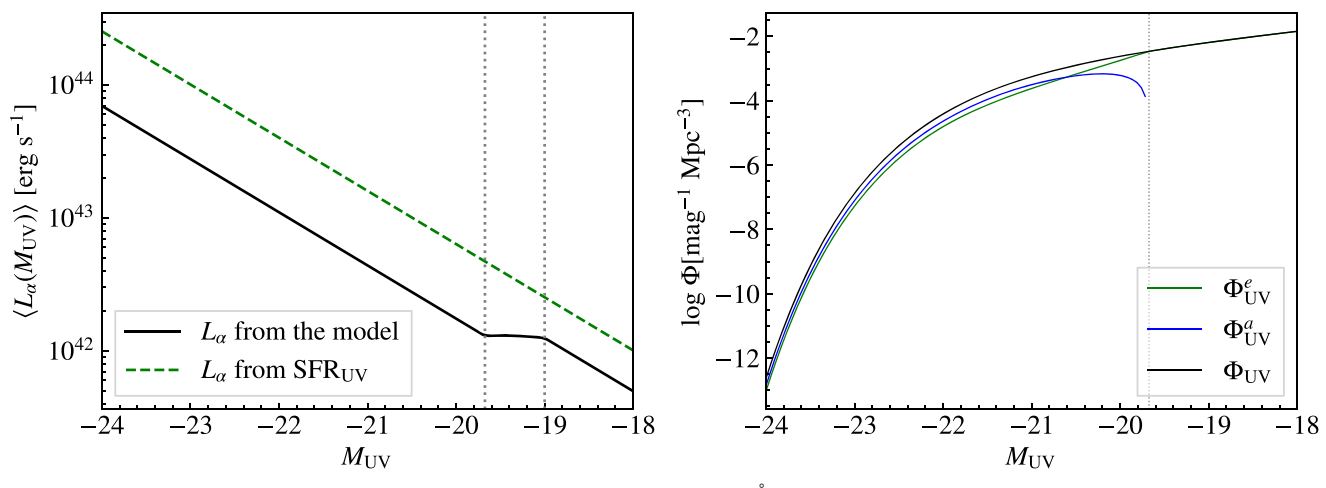


Figure 15. Left: Mean Ly α luminosity $\langle L_{\alpha}(M_{\rm UV}) \rangle$ within the 2" aperture of the REW > 0 Å population as a function of the UV magnitude $M_{\rm UV}$, as presented in Equation (B8). The gray dotted lines denote the turning points of a_1 as expressed in Equation (B3). The green dashed line denotes the expected Ly α luminosity for the SFR associated with the UV luminosity. Right: UV LF of the REW < 0 Å population $\Phi_{\rm UV}^a$, the REW > 0 Å population $\Phi_{\rm UV}^e$, and the entire population $\Phi_{\rm UV}$ as a function of $M_{\rm UV}$, as presented in Equations (B6) and (B7). We take the Reddy & Steidel (2009) UV LF as an example. The gray dotted line denotes one of the turning points of a_1 (Equation (B3)), where $a_1 = 0$ and the REW remains larger than 0 as $M_{\rm UV}$ increases. That is, we assume that there is no REW < 0 Å population over this $M_{\rm UV}$ range, which will lead to an underestimation of the total Ly α luminosity.

In addition, the net absorption from the REW < 0 population will make a negative contribution. The "absorbed" luminosity could be described as

$$\langle L_{\alpha}^{\text{Abs}}(M_{\text{UV}})\rangle = \frac{\int_{-\infty}^{0} L_{\alpha}(\text{REW}, M_{\text{UV}}) P(\text{REW}|M_{\text{UV}}) d\text{REW}}{\int_{-\infty}^{0} P(\text{REW}|M_{\text{UV}}) d\text{REW}},$$
(B9)

which would yield a negative value.

The contribution to the Ly α luminosity density from the inner part comes from the emission of the REW > 0 population and the absorption of the REW < 0 population, which is

$$\rho_{\text{Ly}\alpha}^{\text{inner}} = \int_{M_{\text{UV,min}}}^{M_{\text{UV,max}}} \left[\langle L_{\alpha}(M_{\text{UV}}) \rangle \Phi_{\text{UV}}^{e}(M_{\text{UV}}) + \langle L_{\alpha}^{\text{Abs}}(M_{\text{UV}}) \rangle \Phi_{\text{UV}}^{a}(M_{\text{UV}}) \right] dM_{\text{UV}}.$$
(B10)

In our model the negative absorption component is actually insignificant compared to the emission one, with the former being about 1%–4% of the latter depending on the adopted UV LF.

Based on the finding in Steidel et al. (2011), we assume that the $Ly\alpha$ luminosity in the diffuse halo component is the same as that from the central aperture in the REW > 0 population and that the diffuse component in the REW < 0 population takes the same value at any given UV luminosity. Then the contribution from the outer part $Ly\alpha$ emission of the REW > 0 population has the same expression as in the above equation, while that from the REW < 0 population is obtained by replacing Φ^e_{UV} with Φ^a_{UV} . The total outer part contribution from $Ly\alpha$ halos is then

$$\rho_{\mathrm{Ly}\alpha}^{\mathrm{outer}} = \int_{M_{\mathrm{UV,min}}}^{M_{\mathrm{UV,max}}} \langle L_{\alpha}(M_{\mathrm{UV}}) \rangle \Phi_{\mathrm{UV}}(M_{\mathrm{UV}}) dM_{\mathrm{UV}}.$$
 (B11)

We adopt $M_{\rm UV,min} = -24$ and $M_{\rm UV,max} = -12$ in our calculation.

The outer part Ly α emission can have contributions from satellite galaxies in high-mass halos (e.g., Lake et al. 2015; Momose et al. 2016; Mitchell et al. 2021), while the UV LF

used to compute the inner part Ly α emission should already include the satellite population. Therefore, in our model there is a possibility of double-counting the contribution of Ly α emission from the satellites. From halo modeling of LBG clustering, Cooray & Ouchi (2006) found that the contribution from satellites to the UV LF is at a level of $\sim 10^{-3}$ – 10^{-2} over a wide luminosity range and that it becomes even lower at the faint end ($M_{\rm UV} > -17$). A similar result was also obtained by Jose et al. (2013). These empirical results suggest that the contribution of satellite galaxies to the total cosmic Ly α luminosity density is negligible, and we simply ignore the effect induced by possibly double-counting satellites here.

Note that our model is just a rough estimate of the total $Ly\alpha$ luminosity, with systematics arising from both the $Ly\alpha$ REW PDF and the UV LFs. For example, the Dijkstra & Wyithe (2012) REW PDF may underpredict the number of large-REW systems, leading to an underestimate of the total $Ly\alpha$ luminosity. On the other hand, the modeled REW PDF may not describe the number of galaxies with net absorption very well. However, these uncertainties would not change our main claim significantly. Future observations of UV luminosity dependent $Ly\alpha$ REW distribution and measurements of UV LFs are expected to improve the modeling.

ORCID iDs

Xiaojing Lin https://orcid.org/0000-0001-6052-4234 Zheng Zheng https://orcid.org/0000-0003-1887-6732 Zheng Cai https://orcid.org/0000-0001-8467-6478

References

Ahumada, R., Prieto, C. A., Almeida, A., et al. 2020, ApJS, 249, 3
Anderson, C. J., Luciw, N. J., Li, Y. C., et al. 2018, MNRAS, 476, 3382
Arrigoni Battaia, F., Hennawi, J. F., Cantalupo, S., & Prochaska, J. X. 2016, ApJ, 829, 3

Arrigoni Battaia, F., Hennawi, J. F., Prochaska, J. X., et al. 2018, MNRAS, 482, 3162

Bacon, R., Accardo, M., Adjali, L., et al. 2010, Proc. SPIE, 7735, 773508
Bacon, R., Mary, D., Garel, T., et al. 2021, A&A, 647, A107
Bautista, J. E., Busca, N. G., Guy, J., et al. 2017, A&A, 603, A12
Behroozi, P., Wechsler, R. H., Hearin, A. P., & Conroy, C. 2019, MNRAS, 488, 3143

```
Blomqvist, M., du Mas des Bourboux, H., Busca, N. G, et al. 2019, A&A,
   629, A86
Bolton, A. S., Schlegel, D. J., Aubourg, É., et al. 2012, AJ, 144, 144
Borisova, E., Cantalupo, S., Lilly, S. J., et al. 2016, ApJ, 831, 39
Bouwens, R. J., Illingworth, G. D., Oesch, P. A., et al. 2015, ApJ, 803, 34
Brodzeller, A., & Dawson, K. 2022, AJ, 163, 110
Cai, Z., Fan, X., Bian, F., et al. 2017, ApJ, 839, 131
Cai, Z., Hamden, E., Matuszewski, M., et al. 2018, ApJL, 861, L3
Cai, Z., Cantalupo, S., Prochaska, J. X., et al. 2019, ApJS, 245, 23
Cannon, R., Drinkwater, M., Edge, A., et al. 2006, MNRAS, 372, 425
Cantalupo, S., Arrigoni-Battaia, F., Prochaska, J. X., Hennawi, J. F., &
  Madau, P. 2014, Natur, 506, 63
Cantalupo, S., Porciani, C., & Lilly, S. J. 2008, ApJ, 672, 48
Cantalupo, S., Porciani, C., Lilly, S. J., & Miniati, F. 2005, ApJ, 628, 61
Chiang, Y.-K., Ménard, B., & Schiminovich, D. 2019, ApJ, 877, 150
Cooray, A., & Ouchi, M. 2006, MNRAS, 369, 1869
Croft, R. A. C., Miralda-Escudé, J., Zheng, Z., Blomqvist, M., & Pieri, M.
   2018, MNRAS, 481, 1320
Croft, R. A. C., Miralda-Escudé, J., Zheng, Z., et al. 2016, MNRAS, 457, 3541
de La Vieuville, G., Bina, D., Pello, R., et al. 2019, A&A, 628, A3
de La Vieuville, G., Pelló, R., Richard, J., et al. 2020, A&A, 644, A39
DESI Collaboration, Aghamousa, A., Aguilar, J., et al. 2016, arXiv:1611.
  00036
Dijkstra, M., & Wyithe, J. S. B. 2012, MNRAS, 419, 3181
Drake, A. B., Garel, T., Wisotzki, L., et al. 2017a, A&A, 608, A6
Drake, A. B., Guiderdoni, B., Blaizot, J., et al. 2017b, MNRAS, 471, 267
du Mas des Bourboux, H, Dawson, K. S., Busca, N. G, et al. 2019, ApJ,
   878, 47
du Mas des Bourboux, H, Rich, J., Font-Ribera, A., et al. 2020, ApJ, 901, 153
Eisenstein, D. J., Annis, J., Gunn, J. E., et al. 2001, AJ, 122, 2267
Elias, L. M., Genel, S., Sternberg, A., et al. 2020, MNRAS, 494, 5439
Font-Ribera, A., Arnau, E., Miralda-Escudé, J., et al. 2013, JCAP, 2013, 018
Fumagalli, M., O'Meara, J. M., & Prochaska, J. X. 2011, Sci, 334, 1245
Gallego, S. G., Cantalupo, S., Lilly, S., et al. 2018, MNRAS, 475, 3854
Gallego, S. G., Cantalupo, S., Sarpas, S., et al. 2021, MNRAS, 504, 16
Giavalisco, M., Vanzella, E., Salimbeni, S., et al. 2011, ApJ, 743, 95
Górski, K. M., Hivon, E., Banday, A. J., et al. 2005, ApJ, 622, 759
Gould, A., & Weinberg, D. H. 1996, ApJ, 468, 462
Hamilton, A. J. S. 1992, ApJL, 385, L5
Hawkins, E., Maddox, S., Cole, S., et al. 2003, MNRAS, 346, 78
Heneka, C., Cooray, A., & Feng, C. 2017, ApJ, 848, 52
Hennawi, J. F., Prochaska, J. X., Cantalupo, S., & Arrigoni-Battaia, F. 2015,
    ci, 348, 779
Ho, M.-F., Bird, S., & Garnett, R. 2021, MNRAS, 507, 704
Hu,\,W.,\,Wang,\,J.,\,Zheng,\,Z.\text{-}Y.,\,et\,\,al.\,\,2019,\,{\color{red}ApJ},\,{\color{blue}886},\,{\color{blue}90}
Jose, C., Subramanian, K., Srianand, R., & Samui, S. 2013, MNRAS,
   429, 2333
Kaiser, N. 1987, MNRAS, 227, 1
Kennicutt, R. C. J 1998, ARA&A, 36, 189
Kollmeier, J. A., Zheng, Z., Davé, R., et al. 2010, ApJ, 708, 1048
Kovetz, E. D., Viero, M. P., Lidz, A., et al. 2017, arXiv:1709.09066
Kusakabe, H., Verhamme, A., Blaizot, J., et al. 2022, A&A, 660, A44
Lake, E., Zheng, Z., Cen, R., et al. 2015, ApJ, 806, 46
```

```
Leclercq, F., Bacon, R., Wisotzki, L., et al. 2017, A&A, 608, A8
Li, Z., Steidel, C. C., Gronke, M., & Chen, Y. 2021, MNRAS, 502, 2389
Lujan Niemeyer, M., Komatsu, E., Byrohl, C., et al. 2022, ApJ, 929, 90
Lyke, B. W., Higley, A. N., McLane, J. N., et al. 2020, ApJS, 250, 8
Masui, K. W., Switzer, E. R., Banavar, N., et al. 2013, ApJL, 763, L20
Matsuda, Y., Yamada, T., Hayashino, T., et al. 2004, AJ, 128, 569
Matsuda, Y., Yamada, T., Hayashino, T., et al. 2011, MNRAS, 410, L13
Matsuda, Y., Yamada, T., Hayashino, T., et al. 2012, MNRAS, 425, 878
McCarthy, K. S., Zheng, Z., & Guo, H. 2019, MNRAS, 487, 2424
Mitchell, P. D., Blaizot, J., Cadiou, C., et al. 2021, MNRAS, 501, 5757
Momose, R., Ouchi, M., Nakajima, K., et al. 2014, MNRAS, 442, 110
Momose, R., Ouchi, M., Nakajima, K., et al. 2016, MNRAS, 457, 2318
Morrissey, P., Matuszewski, M., Martin, D. C., et al. 2018, ApJ, 864, 93
Moster, B. P., Naab, T., & White, S. D. M. 2013, MNRAS, 428, 3121
Moster, B. P., Somerville, R. S., Maulbetsch, C., et al. 2010, ApJ, 710, 903
Noterdaeme, P., Petitjean, P., Carithers, W. C., et al. 2012, A&A, 547, L1
Ouchi, M., Shimasaku, K., Akiyama, M., et al. 2008, ApJS, 176, 301
Ouchi, M., Shimasaku, K., Furusawa, H., et al. 2010, ApJ, 723, 869
Pâris, I., Petitjean, P., Aubourg, É., et al. 2018, A&A, 613, A51
Parsa, S., Dunlop, J. S., McLure, R. J., & Mortlock, A. 2016, MNRAS,
   456, 3194
Percival, W. J., & White, M. 2009, MNRAS, 393, 297
Planck Collaboration, Aghanim, N., Akrami, Y., et al. 2020, A&A, 641, A6
Reddy, N. A., & Steidel, C. C. 2009, ApJ, 692, 778
Reid, B., Ho, S., Padmanabhan, N., et al. 2015, MNRAS, 455, 1553
Robertson, B. E., Ellis, R. S., Furlanetto, S. R., & Dunlop, J. S. 2015, ApJL,
   802, L19
Ross, N. P., McGreer, I. D., White, M., et al. 2013, ApJ, 773, 14
Sawicki, M. 2012, MNRAS, 421, 2187
Seljak, U. 2012, JCAP, 2012, 004
Shapley, A. E., Steidel, C. C., Pettini, M., & Adelberger, K. L. 2003, ApJ,
Silva, M. B., Kooistra, R., & Zaroubi, S. 2016, MNRAS, 462, 1961
Silva, M. B., Santos, M. G., Gong, Y., Cooray, A., & Bock, J. 2013, ApJ,
   763, 132
Sobral, D., Santos, S., Matthee, J., et al. 2018, MNRAS, 476, 4725
Sobral, D., Smail, I., Best, P. N., et al. 2013, MNRAS, 428, 1128
Steidel, C. C., Adelberger, K. L., Shapley, A. E., et al. 2000, ApJ, 532, 170
Steidel, C. C., Bogosavljević, M., Shapley, A. E., et al. 2011, ApJ, 736, 160 Tramonte, D., & Ma, Y.-Z. 2020, MNRAS, 498, 5916
Tramonte, D., Ma, Y.-Z., Li, Y.-C., & Staveley-Smith, L. 2019, MNRAS,
   489, 385
Véron-Cetty, M. P., & Véron, P. 2010, A&A, 518, A10
Wisotzki, L., Bacon, R., Blaizot, J., et al. 2016, A&A, 587, A98
Wisotzki, L., Bacon, R., Brinchmann, J., et al. 2018, Natur, 562, 229
Witstok, J., Puchwein, E., Kulkarni, G., Smit, R., & Haehnelt, M. G. 2021,
   A&A, 650, A98
Wold, I. G. B., Finkelstein, S. L., Barger, A. J., Cowie, L. L., &
   Rosenwasser, B. 2017, ApJ, 848, 108
Xue, R., Lee, K.-S., Dey, A., et al. 2017, ApJ, 837, 172
Zheng, Z., Cen, R., Trac, H., & Miralda-Escudé, J. 2011a, ApJ, 726, 38
Zheng, Z., Cen, R., Weinberg, D., Trac, H., & Miralda-Escudé, J. 2011b, ApJ,
   739, 62
```